Mechanics of hot isostatic pressing in intermetallic matrix composites

Y. A. BAHEI-EL-DIN
Structural Engineering Department, Cairo University, Giza, Egypt

G. J. DVORAK, J. F. WU*
Department of Civil and Environmental Engineering, Rensselaer Polytechnic Institute, Troy, NY 12180, USA

Thermal residual and mechanical stresses generated by hot isostatic pressing, cooling and subsequent mechanical loading of SCS6/Ni$_3$Al and SCS6/Ti$_3$Al composites with uncoated and carbon-coated fibres have been simulated by micromechanical modelling. The solutions were found in a periodic hexagonal array model of the microstructure with the finite element method. The intermetallic matrices were assumed to be elastic–plastic, with temperature-dependent properties. The fibre and coating were assumed to be elastic. Local stress fields and overall response were found for several processing sequences. The results suggest that plastic deformation of the matrix during cooling from fabrication temperatures reduces residual stresses. The Ni$_3$Al matrix system yields more easily than the Ti$_3$Al system. HIP programmes that promote such yielding are proposed and analysed in both systems. Compliant and expansive fibre coatings tend to reduce the thermal stresses, but may also enhance the interface stresses in the matrix under overall mechanical loads.

1. Introduction
One of the factors affecting the overall response and damage and failure resistance of composite materials is the residual stress field caused by pressure and temperature histories applied in fabrication, processing and subsequent cooling. The distribution and magnitude of such stresses is affected by the thermomechanical compatibility of the phases, and by the inelastic deformation that may take place under certain loading conditions in some systems. Understanding of the various factors involved is possible only with reasonably detailed modelling of the fabrication, processing and loading sequences.

The present work examines local stresses in SCS6/Ni$_3$Al and SCS6/Ti$_3$Al intermetallic matrix composites reinforced by coated and uncoated fibres, under thermal changes, mechanical loads, and thermomechanical loading conditions which simulate fabrication by hot isostatic pressing (HIP). The effect of fibre coating, matrix plasticity, and standard and modified HIP parameters is considered. The results focus primarily on understanding the mechanics of the HIP process and the role of the various parameters involved.

Section 2 describes the micromechanical model used in this study and the constitutive equations of the phases; Section 3 presents the material properties of the phases. The local stress concentrations found in unidirectional composites reinforced by coated and uncoated fibres under mechanical or thermal loads are presented in Section 4. The main results of interest appear in Section 5, where we evaluate the stresses created in the two systems during standard and modified hot isostatic pressing proce-dures, and in subsequent mechanical loading or reheating to processing temperatures. Significantly different outcomes are found for different HIP parameters. Interpretation of the results by several models shows that higher pressures and axisymmetric rather than isotropic overall stress states promote plastic straining of the matrix and thus help to reduce the magnitudes of the residual fields.

2. Evaluation of local fields in fibrous media

2.1. Micromechanical models
The overall response and local fields in fibrous composites can be predicted by several material models which offer various approximations of the microgeometry, phase constitutive behaviour, and loading conditions. In elastic composites, the local moduli do not change during deformation, hence acceptable estimates can be found using approaches that rely on averages of local fields in the phases, such as the self-consistent [1] or Mori–Tanaka [2–4] models. Analogous techniques are available for inelastic composites. However, because the instantaneous moduli

---

*Present address: ABS Americas, The American Bureau of Shipping, 263 North Belt East, Houston, TX 77060, USA.

of the inelastic phases depend on the local deformation history, the overall response may not be well represented by averages of the local fields. Indeed, a recent comparison [5] of several micromechanical models with experiments indicated substantial deviations of certain predictions from observed behaviour. This was true in particular for the self-consistent and Mori-Tanaka models. Our bimodal plasticity theory [6] provided good predictions of the observed yield surfaces, but not of overall plastic strains. This is readily understood if the overall surface is regarded as a locus of vertices of yield cones formed by clusters of yield surfaces of matrix subelements in the overall stress space, so that the plastic strain increment vectors are contained within cones of normals at each loading point [7]. Most reliable predictions are offered by models that can approximate the actual local stress and strain fields. Those are typically discretized unit cell models, such as the periodic hexagonal array model [8, 9], or its rectangular array analogous [10, 11]. Under remotely applied uniform stress or strain, one can identify a representative unit cell, derive periodic boundary conditions for the cell, discretize the volume and evaluate the local fields in terms of piecewise-uniform estimates by the finite element method or by the transformation field analysis [12]. A survey of the above models can be found in the reviews by Bahei-El-Din and Dvorak [13] and Dvorak [14].

The present work employs the periodic hexagonal array (PHA) model developed by Dvorak and Teply [8, 9]. In a series of recent publications, advanced constitutive equations for elastic-plastic and viscoplastic phases have been implemented in this model [15, 16] and predictions were verified by comparisons with experimental results [5, 16–19]. The microstructural geometry in the transverse plane of a unidirectionally reinforced fibrous composite is represented by a periodic distribution of the fibres in a hexagonal array. The fibre cross-sections are approximated by

$(n \times 6)$-sided polygons. Examples of the PHA microgeometry with hexagonal and dodecagonal fibre cross-sections are shown in Fig. 1. The hexagonal array is divided into two kinds of unit cell, as indicated by the shaded and unshaded triangles. Under overall uniform stresses or strains, the internal fields of the two sets of unit cells are related by a simple transformation. Accordingly, for uniform overall stresses or strains applied to the aggregate, only one unit cell selected from either set needs to be analysed under certain displacement boundary conditions which reflect periodicity of the local fields [9]. A three-dimensional view of the unit cell showing dimensions and support conditions is given in Fig. 2 for a fibre with hexagonal cross-section.

The actual analysis was performed by the finite element method. The unit cell was subdivided into a selected number of subelements in the matrix, fibre, and coating subdomains. The degree of mesh refinement may vary from a few elements in each subdomain to several hundred elements. In general, evaluation of the internal fields in the phases and at their interfaces requires a large number of elements [20], whereas the overall response can be adequately predicted with few elements [15, 20]. Examples of various degrees of mesh refinements are shown in Fig. 3. In the present study we implemented the PHA microgeometry in the ABAQUS finite element program [21] for the mesh shown in Fig. 3b.

2.2. Phase constitutive equations

The fibre and coating, if any, are assumed to be elastic and transversely isotropic. The matrix is assumed to be isotropic in the elastic deformation range confined within a current yield surface. The thermoelastic properties of the phases are, in general, functions of temperature. Using contracted notation, let $d\sigma_r = [d\sigma_1\, d\sigma_2\ d\sigma_3\, d\sigma_4\, d\sigma_5\, d\sigma_6]^T$, $d\varepsilon_r = [d\varepsilon_1\, d\varepsilon_2\ d\varepsilon_3\, d\varepsilon_4\, d\varepsilon_5\, d\varepsilon_6]^T$, denote the stress and strain
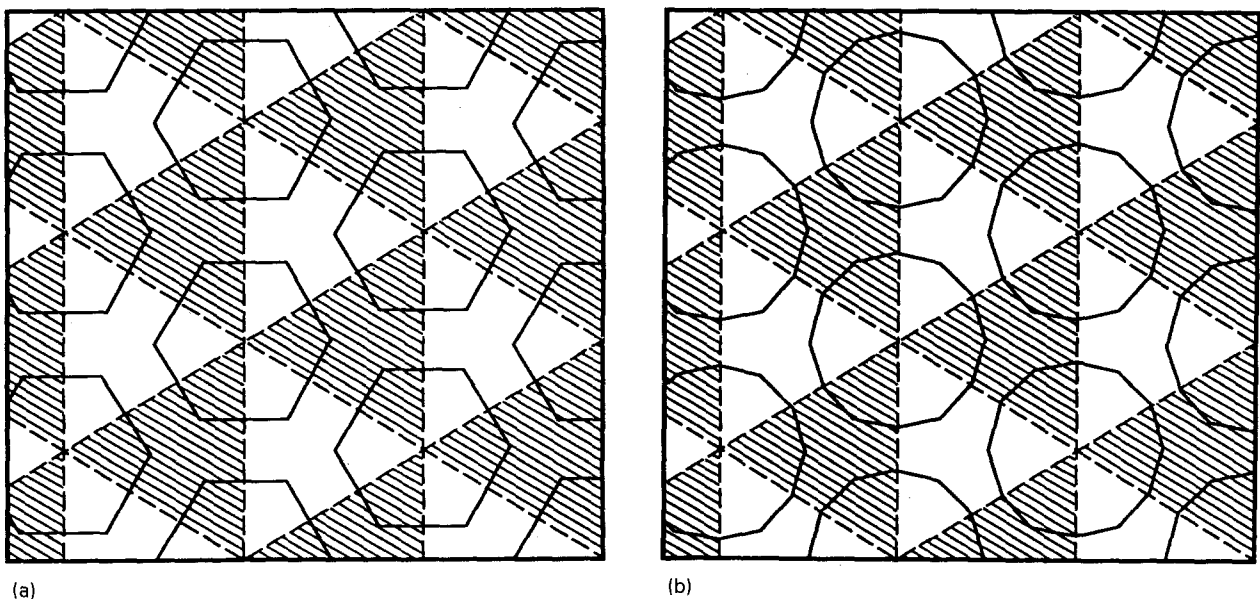

(a) (b)

Figure 1 Transverse cross sections of the PHA microgeometry wtih (a) hexagonal and (b) dodecagonal cylindrical fibres.
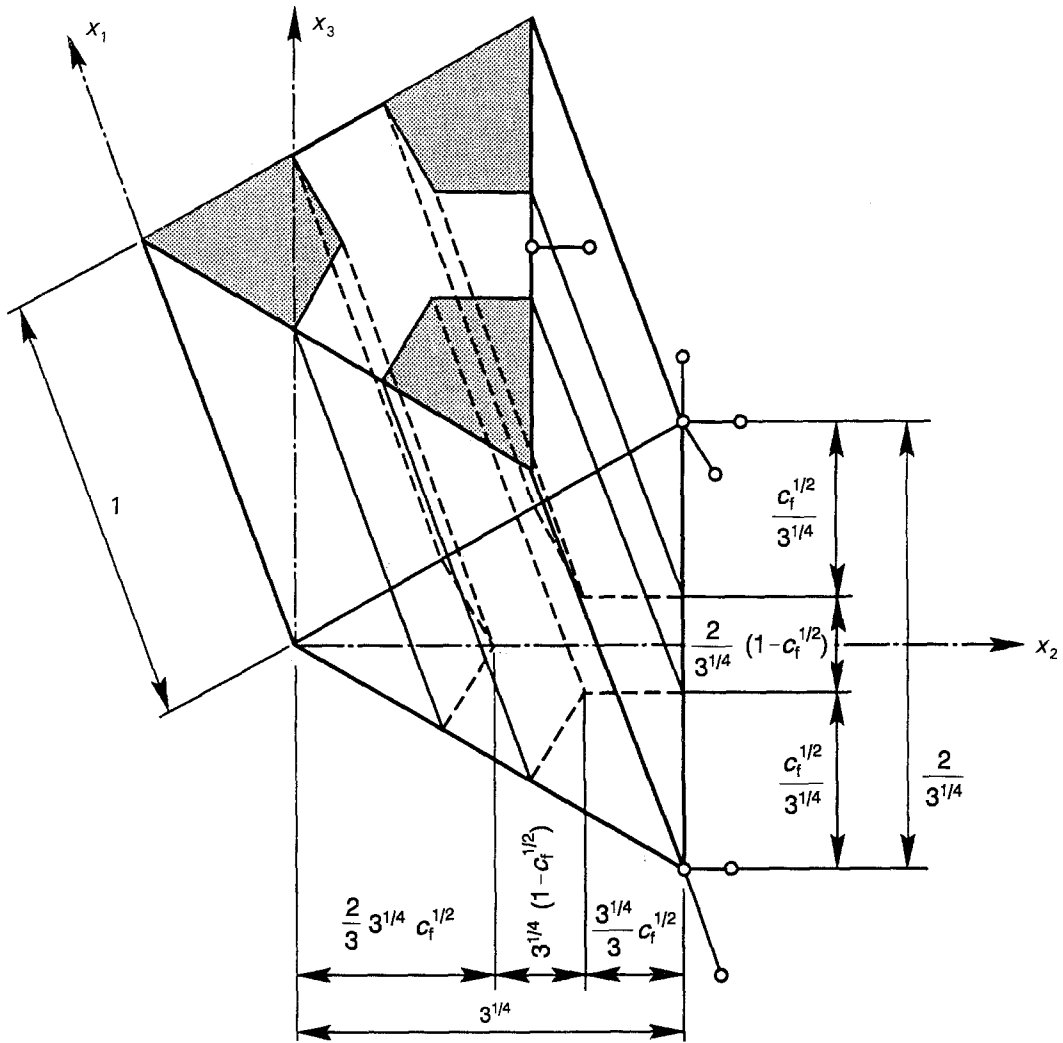
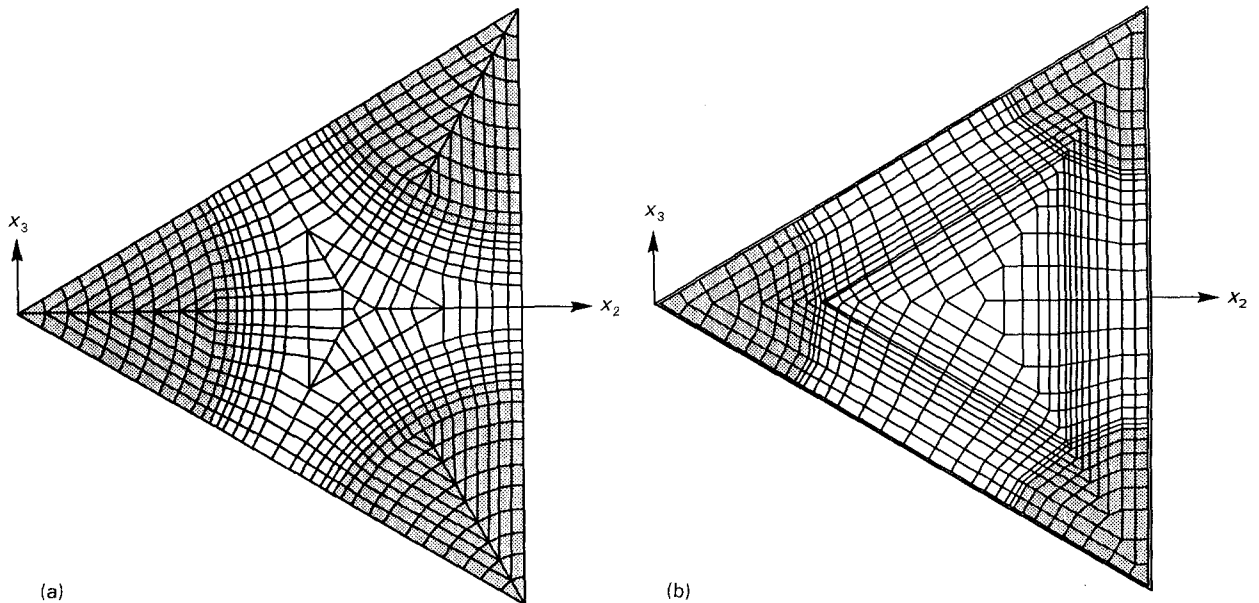Figure 2 Geometry, dimensions and support conditions of the unit cell.

Figure 3 Examples of finite element meshes in the PHA unit cell.

increments in the fibre $r = f$, matrix $r = m$, or the coating $r = c$, in a Cartesian coordinate system x_j, $j = 1, 2, 3$. In the presence of a temperature change, dT, the stress–strain relation for the elastic phases are written in the incremental form [22, 23]

$$d\varepsilon_r = M_r^e(T)\,d\sigma_r + \tilde{m}_r^e(T, \sigma_r)\,dT \qquad (1)$$

$$d\sigma_r = L_r^e(T)\,d\varepsilon_r + \tilde{l}_r^e(T, \varepsilon_r)\,dT \qquad (2)$$

3

where

$$\tilde{m}_r^e(T, \boldsymbol{\sigma}_r) = (\partial M_r^e/\partial T)\boldsymbol{\sigma}_r + m_r^e(T) \quad (3)$$

$$\tilde{l}_r^e(T, \boldsymbol{\varepsilon}_r) = (\partial L_r^e/\partial T)\left[\boldsymbol{\varepsilon}_r - \int_{T_0}^{T} m_r(T)\,dT\right] - L_r^e(T)m_r(T)$$

$$= - L_r^e(T)\tilde{m}_r^e(T) \quad (4)$$

where $L_r^e(T)$ is the phase elastic stiffness matrix, $M_r^e(T) = [L_r^e(T)]^{-1}$ is the elastic compliance matrix, $m_r(T) = [\alpha_A\, \alpha_T\, \alpha_T\, 0\, 0\, 0]^T$ is the thermal strain vector of linear thermal expansion coefficients for the axial and transverse directions, and T_0 is the initial temperature. The dependence of the thermal strain on the current stress in Equation 3 satisfies the path independence requirement of the elastic solution. When integrated along the thermal loading path, Equations 1–4 provide uncoupled mechanical and thermal fields.

For a transversely isotropic phase with the axis of rotational symmetry x_1, the non-zero coefficients of the upper half of the symmetric stiffness matrix, L_r^e, at a given temperature are evaluated as

$$L_{11} = n, \quad L_{22} = L_{33} = k + m, \quad L_{12} = L_{13} = l$$
$$L_{23} = k - m, \quad L_{44} = m, \quad L_{55} = L_{66} = p \quad (5)$$

The Hill's moduli [24] k, l, n, m, and p of the phase are related to the engineering moduli by the relations

$$k = -1/[(4/E_T) - (1/G_T) - (4v_L^2/E_T)] \quad l = 2kv_L$$
$$n = E_L + l^2/k, \quad m = G_T, \quad p = G_L \quad (6)$$

where the Young's modulus, E_L, shear modulus, G_L, the Poisson's ratio, v_L, refer to straining in the longitudinal direction, and E_T, G_T, $v_T = (E_T/2G_T - 1)$ to the transverse plane.

The region of the elastic response of the matrix to thermomechanical loads is determined by certain conditions related to the existence of a yield surface $f(\boldsymbol{\sigma}_m, T) = 0$. Assuming kinematic and isotropic hardening, the Mises yield surface is given by

$$f(\boldsymbol{\sigma}_m, T) \equiv \tfrac{3}{2}(s_m - \boldsymbol{\alpha}_m):(s_m - \boldsymbol{\alpha}_m)$$
$$- (Y(T) + Q)^2 = 0 \quad (7)$$

where s_m is the matrix deviatoric stress, $\boldsymbol{\alpha}_m$ is the centre of the yield surface, Y is the matrix yield stress in simple tension, and Q is isotropic stress function. In Equation 7, we used the notation $(a:b)$ to denote the inner product of second order tensors a_{ij} and b_{ij}.

In particular, elastic response of the matrix obtains if $f < 0$, or if $f = 0$ and $[(\partial f/\partial\boldsymbol{\sigma}_m):d\boldsymbol{\sigma}_m + (\partial f/\partial T)\,dT] \leqslant 0$ [25]. In this case, Equations 1–6 apply and the Hill's moduli in Equation 6 are given in terms of the bulk modulus, K_m, and shear modulus, G_m, of the isotropic matrix as $k = G/(1 - 2v)$, $l = K - 2G/3$, $n = K + 4G/3$, $m = p = G$.

Elastic–plastic deformation takes place in the matrix if $f = 0$ and $[(\partial f/\partial\boldsymbol{\sigma}_m):d\boldsymbol{\sigma}_m + (\partial f/\partial T)\,dT] > 0$. The assumption is that the total strain increment can be additively decomposed into elastic and plastic components. The instantaneous response is then evaluated from Equations 1 and 2, providing that the elastic compliance matrix M_r^e, the stiffness matrix L_r^e, the thermal strain vector, $\tilde{m}_r^e$, and the thermal stress vector, $\tilde{l}_r^e$, are replaced by their instantaneous counter-

parts. The latter are written as [22, 26]

$$M_m = M_m^e + (3/2H)(n:n^T) \quad (8)$$

$$L_m = L_m^e - [2G_m/(1 + H/3G_m)](n:n^T) \quad (9)$$

$$\tilde{m}_m = \tilde{m}_m^e - ([3^{1/2}\,Y'(T)]/(2^{1/2}H))n \quad (10)$$

$$\tilde{l}_m = [2G_m/(1 + H/3G_m)](n^T\tilde{m}_m^e$$
$$+ [Y'(T)/6^{1/2}\,G_m])n - \tilde{l}_m^e \quad (11)$$

$$H = [d\bar{\sigma} - Y'(T)\,dT]/d\bar{\varepsilon}^p \quad (12a)$$

$$d\bar{\sigma} = \left(\frac{3}{2}ds:ds\right)^{1/2} \quad (12b)$$

$$d\bar{\varepsilon}^p = \left(\frac{2}{3}d\varepsilon^p:d\varepsilon^p\right)^{1/2} \quad (12c)$$

$$n = [1/(2/3)^{1/2}\,Y][\bar{s}_{11}\,\bar{s}_{22}\,\bar{s}_{33}\,2\bar{s}_{23}\,2\bar{s}_{31}\,2\bar{s}_{12}]^T$$

$$\bar{s} = \boldsymbol{\sigma}_m - \boldsymbol{\alpha}_m \quad (13)$$

where $Y'(T) = dY/dT$, ε^p is the plastic strain vector, and H is plastic tangent modulus of the stress–plastic strain curve. In Equation 9, $n:n^T$ denotes the tensor product $n_{ij}n_{kl}$.

Evolution of the position of the centre of the matrix yield surface $\boldsymbol{\alpha}_m$, the isotropic function Q, and the plastic tangent modulus H may take several different forms which are usually guided by experimental observations. In the present work we used the constitutive equations available in the ABAQUS finite element program. Specifically, we assumed linear hardening in which H is constant under isothermal loading, and specified translation of the yield surface by the Prager-Ziegler hardening rule. Except for variations of the yield stress Y caused by the temperature change, we neglected isotropic hardening of the yield surface. Other constitutive rules, such as the two-surface plasticity theory [27], could be applied as well; these would provide somewhat different magnitudes of the local fields.

3. The intermetallic matrix composite systems

Two intermetallic matrix composite materials reinforced by aligned continuous fibres are considered in the present study. One system has nickel aluminide (Ni_3Al) matrix, the other a titanium aluminide (Ti_3Al) matrix. Both systems are reinforced by silicon carbide fibre (SCS6) at 25% volume concentration. A 10 μm thick carbon coating has been added to the fibres in some cases. The thermoelastic properties of the silicon carbide fibre and the carbon coating are taken as independent of temperature, and their specific magnitudes are given in Table I [28]. The thermoelastic properties of the two aluminide matrices vary with temperature as shown in Tables II and III [29, 30]. Variation of the Young's moduli and of the thermal expansion coefficients of the phases with temperature is shown in Figs 4 and 5, respectively, together with the Mori–Tanaka estimates of the overall moduli and expansion coefficients derived from these estimates. It is seen that the thermal coefficient mismatch between the phases in the nickel-based composite system is larger than that in the titanium-based system.

4

TABLE I Material properties of SCS6 fibre and carbon coating [28]

	E_L (GPa)	E_T (GPa)	G_L (GPa)	G_T (GPa)	ν_L	α_L $(10^{-6}\,°C^{-1})$	α_T $(10^{-6}\,°C^{-1})$
SCS6 fibre	413.6	413.6	159.1	159.1	0.3	4.6	4.6
Carbon coating	172.4	6.9	14.5	3.8	0.3	1.8	28

TABLE II Material properties of Ni₃Al matrix [29]

θ (°C)	E (GPa)	ν	α $(10^{-6}\,°C^{-1})$	Y (MPa)	H (GPa)
1200	134	0.32	20.6	137	6.70
994	142	0.32	19.0	279	7.10
776	150	0.32	17.2	459	7.50
673	154	0.32	16.4	557	7.70
642	155	0.32	16.1	564	7.75
578	158	0.32	15.6	535	7.90
376	165	0.32	14.3	356	8.25
327	167	0.32	14.0	279	8.35
206	172	0.32	13.4	156	8.60
127	175	0.32	13.0	110	8.75
21	179	0.32	12.5	79	8.95

Figure 5 Coefficients of thermal expansion of the phases and composites. (M–T estimates) (— — —) α_A, (- - -) α_T.

TABLE III Material properties of Ti₃Al matrix [30]

θ (°C)	E (GPa)	ν	α $(10^{-6}\,°C^{-1})$	Y (MPa)	H (GPa)
950	32.4	0.3	10.4	210	2.71
760	51.2	0.3	10.4	240	2.63
649	62.0	0.3	10.4	260	5.44
427	66.3	0.3	10.4	320	5.88
260	66.3	0.3	10.4	390	5.06
21	69.0	0.3	10.4	500	3.91

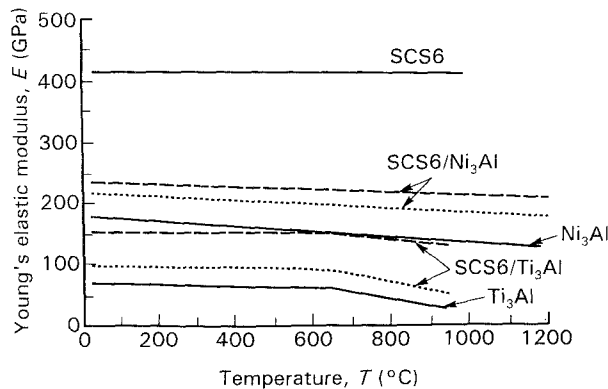*Figure 6* Tensile yield stresses of the matrix materials.

Figure 4 Elastic Young's moduli of the phases and composites (M–T estimates). (— — —) E_A, (- - -) E_T.

The yield stress, Y, and the plastic tangent modulus, H, of the Ni₃Al [29] and the Ti₃Al [30] matrices are shown in Tables II and III as function of temperature. The yield stress changes are shown in Fig. 6. The variation of the yield stress of the Ni₃Al matrix with temperature, which is not typical of intermetallic compounds, will be seen to cause early yielding of the

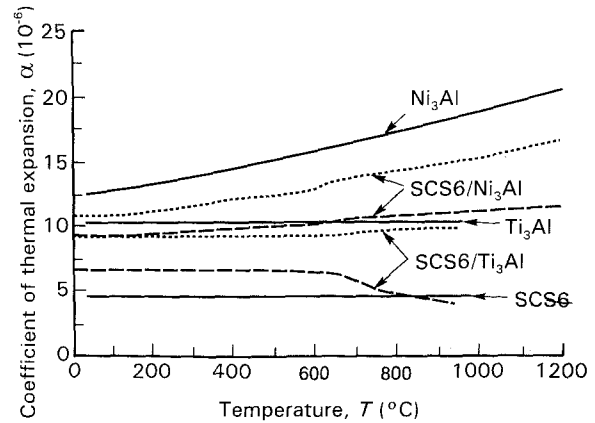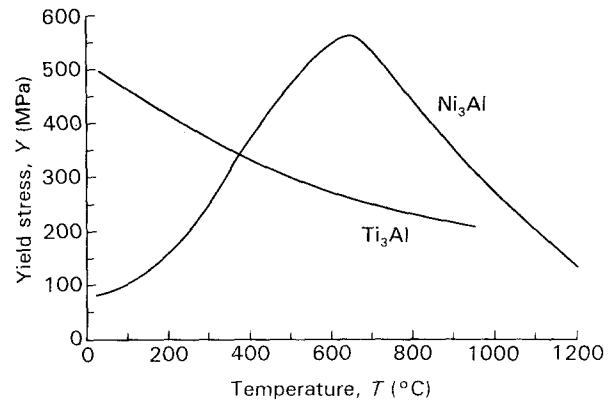nickel-based composite system during fabrication and thus reduce the local stresses in the matrix.

In a typical fabrication process of intermetallic matrix composites, particles of the matrix are sprayed on aligned fibres to create a monolayer composite [31, 32]. The required number of layers is then assembled and encapsulated in a hermetically sealed package consisting of stainless steel plates or tubes depending on the shape of the final product. The assembly is then consolidated by hot isostatic pressing (HIP) at a specified high temperature and hydrostatic pressure. After a predetermined time period, the HIP package is cooled down to room temperature and the pressure is simultaneously reduced to atmospheric pressure. Owing to the thermal mismatch present between the fibre and matrix phases, cooldown from the processing temperature cause internal stresses. Such local stresses may lead to localized effects such as yielding or damage, and thus alter the overall

5

performance of the composite. The following sections examine the local stress field in the two intermetallic matrix composites described above, after certain simple loading programs, and after several typical and modified HIP cycles applied during fabrication and processing. Modification of the HIP parameters and thermo-mechanical loading/unloading paths is explored to identify conditions that may lead to reduced residual stress fields.

4. Stress concentrations in uncoated and coated fibre systems

4.1. Elastic response

The local fields and the overall thermomechanical response of elastic composites reinforced by coated or uncoated fibres was evaluated by Benveniste et al. [4], Dvorak et al. [23], and Bahei-El-Din and Dvorak [33]. The latter, as well as our present study, also consider the effect of matrix plastic flow on the local stresses and on overall response. This section presents new data for the stresses in the above intermetallic composite systems subjected to thermal and mechanical loading. In contrast to elastic composites with constant moduli, the systems considered here have temperature-dependent properties. Therefore, all results are presented in terms of ratios of increments of local stresses to the increments of overall stress or temperature, at specified temperature. These ratios may be somewhat different at other temperatures, but they illustrate the magnitudes of changes of local fields under overall applied loads.

First, we examine the thermal and mechanical stresses generated in elastic systems at high temperature, and the overall elastic response over a range of temperatures. An initially stress-free state was assumed, and the magnitudes of thermoelastic phase moduli were taken at 1200 and 950 °C for the SCS6/Ni$_3$Al and SCS6/Ti$_3$Al composites, respectively. Small changes in temperature and transverse tensile stress were applied

in separate solutions for the unit cell shown in Fig. 3b, and the local fields were found using the ABAQUS finite element program. Among the six components of the local stress fields, of interest here are the contours of the ratios of the local transverse normal stress $\Delta\sigma_{22}/\Delta T$ in the unit cell, shown in Figs 7 and 8 for systems with Ni$_3$Al and Ti$_3$Al matrices, respectively, and with uncoated and coated SCS6 fibres. Also of interest are the local to overall transverse normal stress ratios at room temperature, plotted in Figs 9 and 10. The dashed triangular boundary shown in Figs 7–10 indicates the unit cell used in the solution. The contours outside the unit cell were found from periodicity of the local stress field. The significant stress ratios found in these plots are listed in the top part of Table IV. Note that the transverse normal stress, σ_{22}, at the interface coincides with the radial normal stress in the x_2-direction, and with the hoop stress perpendicular to the x_3-direction. The magnitudes of these stresses play a significant role in initiation of fibre/matrix debonding and radial cracking in the matrix at the fibre interface, respectively.

The results in Figs 7 and 8 indicate that a decrease in temperature, and the consequent differential dilatation of the phases, cause compressive radial stresses and tensile hoop stresses in the matrix, and compressive radial and hoop stresses in the fibre. Note that as long as the phases remain elastic, the magnitudes of the thermal stresses found in the titanium-based system are much smaller than those found in the nickel-based system. This is consistent with the smaller difference between the coefficients of thermal expansion of the fibre and matrix in the two systems, Fig. 5. Thermomechanical compatibility can be enhanced by applying a compliant coating to the fibre, such as the CVD-deposited carbon coating with properties described in Table I. This causes a significant reduction in the local thermal stresses, particularly at the fibre/matrix interface, Figs 7b and 8b. Compared to the matrix and fibre phases, the carbon coating has
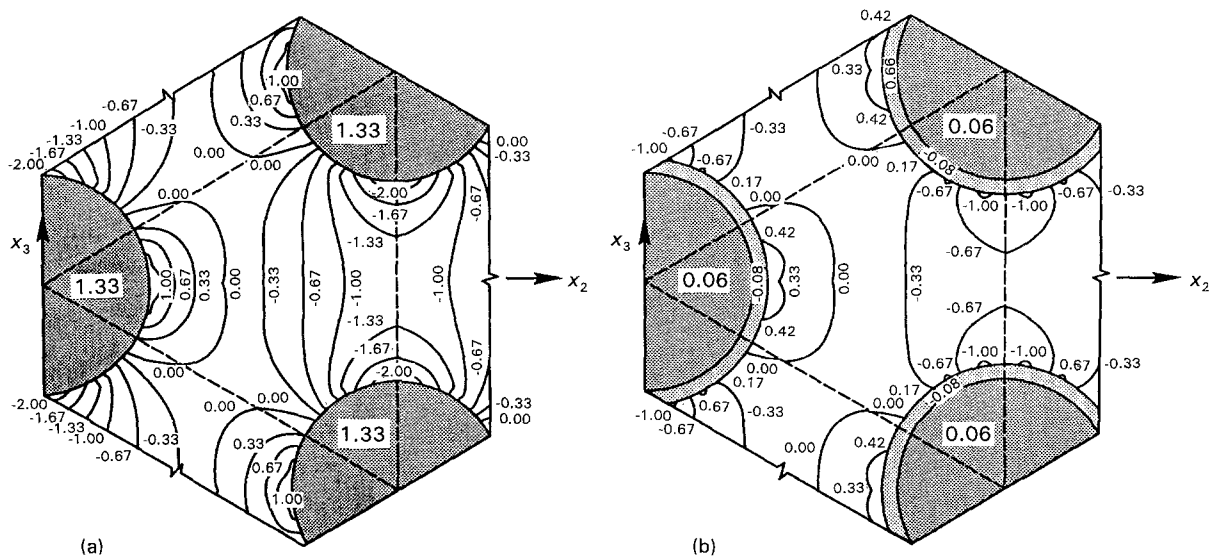

Figure 7 Transverse thermal stress concentrations, $\Delta\sigma_{22}/\Delta T$ (MPa °C^{-1}), in the SCS6/Ni$_3$Al composite in the elastic range at 1200 °C: (a) uncoated fibre, (b) carbon-coated fibre.
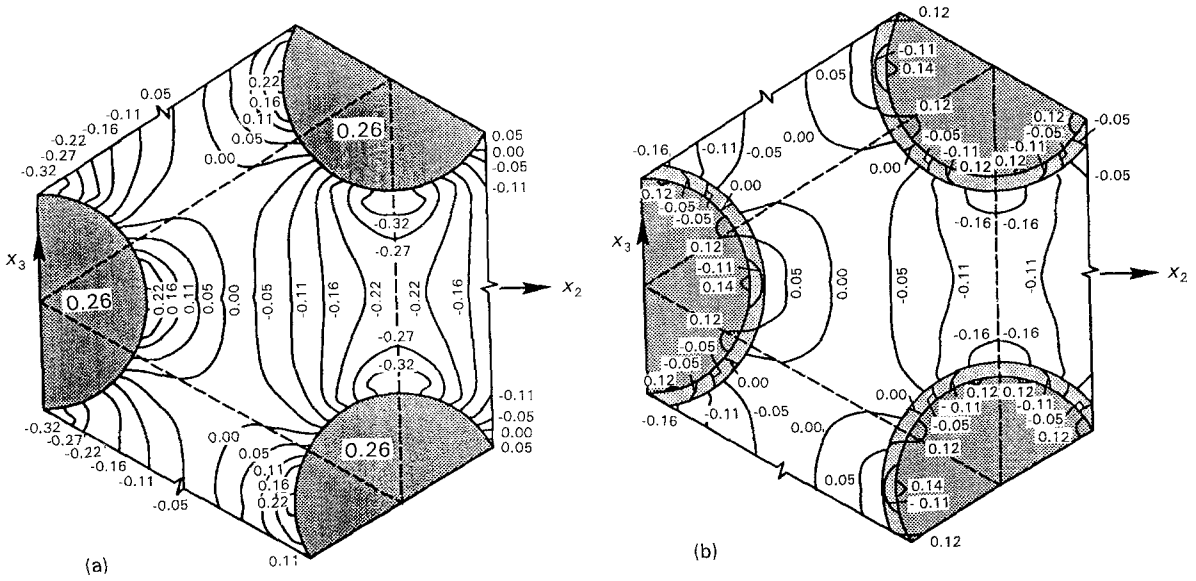
Figure 8 Transverse thermal stress concentrations, $\Delta\sigma_{22}/\Delta T$ (MPa °C^{-1}), in the SCS6/Ti$_3$Al composite in the elastic range at 950 °C: (a) uncoated fibre, (b) carbon-coated fibre.

Figure 9 Transverse mechanical stress concentrations, $\Delta\sigma_{22}/\Delta\bar{\sigma}_{22}$, in the SCS6/Ni$_3$Al composite in the elastic range at 1200 °C: (a) uncoated fibre, (b) carbon-coated fibre.
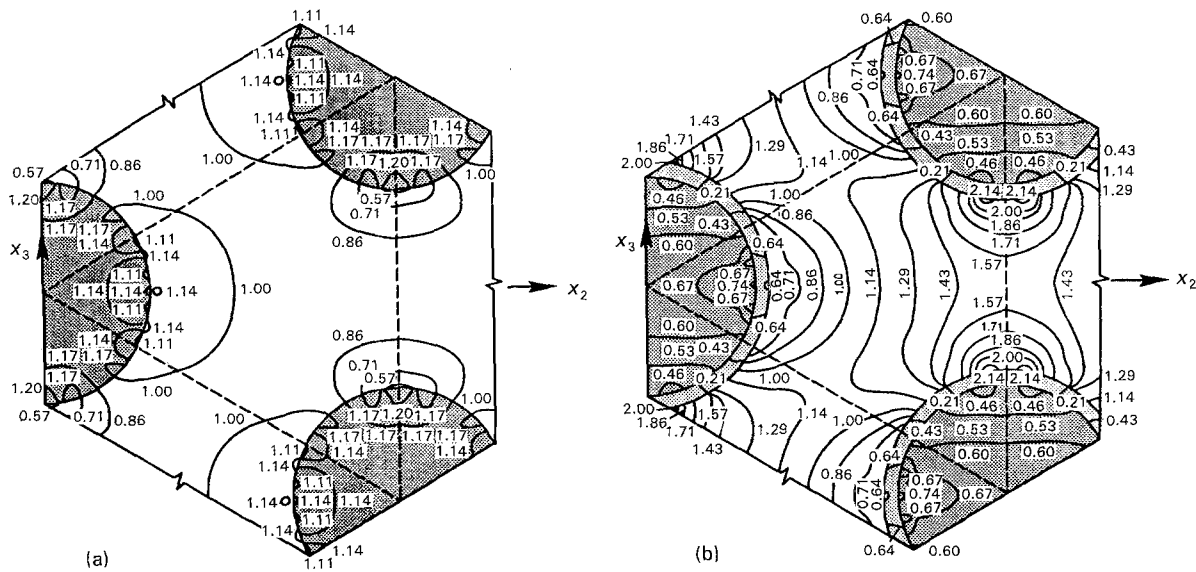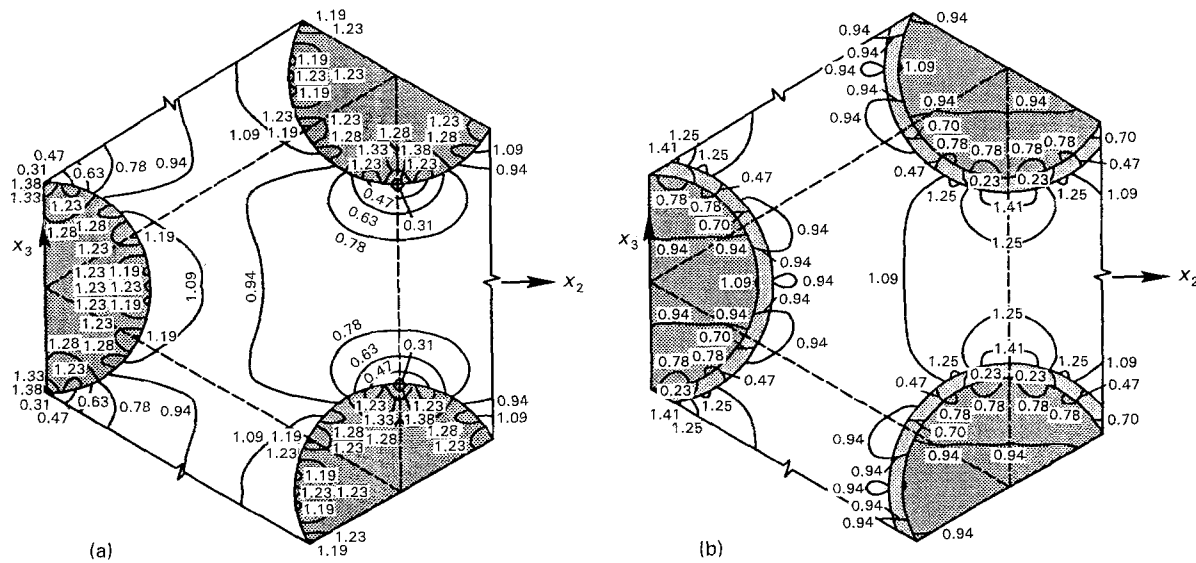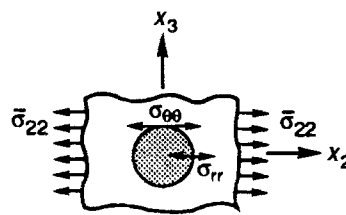

Figure 10 Transverse mechanical stress concentrations, $\Delta\sigma_{22}/\Delta\bar{\sigma}_{22}$, in the SCS6/Ti$_3$Al composite in the elastic range at 950 °C: (a) uncoated fibre, (b) carbon-coated fibre.

TABLE IV Summary of stress concentrations in the matrix at fibre/matrix interface

	SCS6/Ni$_3$Al		SCS6/Ti$_3$Al	
	Uncoated fibre	Coated fibre	Uncoated fibre	Coated fibre
Elastic				
$\Delta\sigma_{rr}/\Delta T^a$ (MPa °C^{-1})	1.56	0.45	0.28	0.08
$\Delta\sigma_{\theta\theta}/\Delta T^a$ (MPa °C^{-1})	-2.13	-0.90	-0.36	-0.18
$\Delta\sigma_{rr}/\Delta\bar{\sigma}_{22}$	1.15	0.61	1.25	0.91
$\Delta\sigma_{\theta\theta}/\Delta\bar{\sigma}_{22}$	0.57	2.01	0.28	1.37
Elastic–Plastic				
$\Delta\sigma_{rr}/\Delta T^a$ (MPa °C^{-1})	0.13	0.08	NY^c	NY^c
$\Delta\sigma_{\theta\theta}/\Delta T^a$ (MPa °C^{-1})	-0.16	-0.13	NY^c	NY^c
$\Delta\sigma_{rr}/\Delta\bar{\sigma}_{22}{}^b$	1.23	1.11	1.28	1.04
$\Delta\sigma_{\theta\theta}/\Delta\bar{\sigma}_{22}{}^b$	0.11	0.56	0.34	0.93

$^a T = 1200\,°C$ in SCS6/Ni$_3$Al, $950\,°C$ in SCS6/Ti$_3$Al.
ΔT(elastic) $= -30\,°C$, ΔT(elastic–plastic) $= T - 21\,°C$.
$^b \bar{\sigma}_{22} = 225$ MPa in SCS6/Ni$_3$Al, 605 MPa in SCS6/Ti$_3$Al.
^{c} No yielding.

a much smaller elastic moduli in the transverse plane, Table I, hence it offers little resistance to lateral thermal deformation of either phase. Also, the coating has a large coefficient of thermal expansion in the transverse plane, and is thus able to fill or vacate the void between the fibre and matrix that expands or contracts with positive or negative changes in temperature.

Contours of the elastic stress concentration factors found in uncoated SCS6/Ni$_3$Al and SCS6/Ti$_3$Al composites under uniform transverse tension are shown in Figs 9 and 10, respectively, for uncoated and coated fibres. The stress concentrations found in both composite systems under overall transverse tension are of similar magnitude. In contrast to its effect under thermal changes, the fibre coating, in general, tends to elevate significantly the mechanical transverse stresses Figs 9b and 10b. In particular, as shown in Table IV, the matrix hoop/transverse overall stress ratio $\Delta\sigma_{\theta\theta}/\Delta\bar{\sigma}_{22}$ increased from 0.57 to 2.01, or by a factor of 3.5 in the SCS6/Ni$_3$Al composite and from 0.28 to 1.37, or by 4.9 in the SCS6/Ti$_3$Al composite when the 10 μm carbon coating was added to the fibre. Of course, the coating reduced both radial stress ratios by similar but not identical magnitudes.

4.2. Elastic–plastic response

The inelastic response of solids to thermomechanical loading depends, in general, on the applied loading path. Therefore, in contrast to the elastic response, it is not possible to find overall moduli, coefficients of thermal expansion, or thermomechanical stress concentrations that are independent of loading history. In what follows we present illustrative examples of inelastic deformation of the two composite systems under monotonically increasing, overall thermal or mechanical loading. In the linearly hardening matrix

assumed herein (cf. Section 2.2), the local instantaneous moduli remain constant during sustained plastic loading along a proportional path, provided, of course, that the yield stress does not change. Therefore, under proportional mechanical loading at constant temperature which causes plastic yielding in all elements of the subdivided unit cell, the local fields change proportionally. This property may be useful in interpretation of the numerical results.

For uniform changes in temperature throughout the volume of the composite, the effect of matrix plastic flow on the local stresses was evaluated for cooldown to room temperature from a stress-free state at 1200 °C for the SCS6/Ni$_3$Al composite and from 950 °C for the SCS6/Ti$_3$Al composite. Along these thermal paths, the nickel-based matrix exhibited extensive plastic deformation, but the titanium-based matrix remained mostly elastic. This is consistent with the variation of the matrix yield stress with temperature shown in Fig. 6.

First, we consider the local stresses in a SCS6/Ni$_3$Al composite. Figs 11–13 show stress contours of the transverse normal stress, σ_{22}, and the transverse shear stress, σ_{23}, found at room temperature in uncoated and carbon-coated fibre systems. Fig. 11 represents the actual field, σ_{22}, and Fig. 12 the same field normalized by the $\Delta T = 1179\,°C$ temperature difference along the cooling path. This was done to facilitate comparisons with the normalized elastic field in Fig. 7. It is seen that the local stress/temperature ratios were reduced substantially by the plastic deformation of the matrix. This can be understood by comparing the Young's moduli, E, with the plastic tangent moduli, H, in Table II. During plastic straining, the matrix becomes very compliant compared to the fibre and can therefore deform at much lower ratios of stress/temperature increments. In fact, the stiffness of the matrix in the plastic range is approximately comparable to
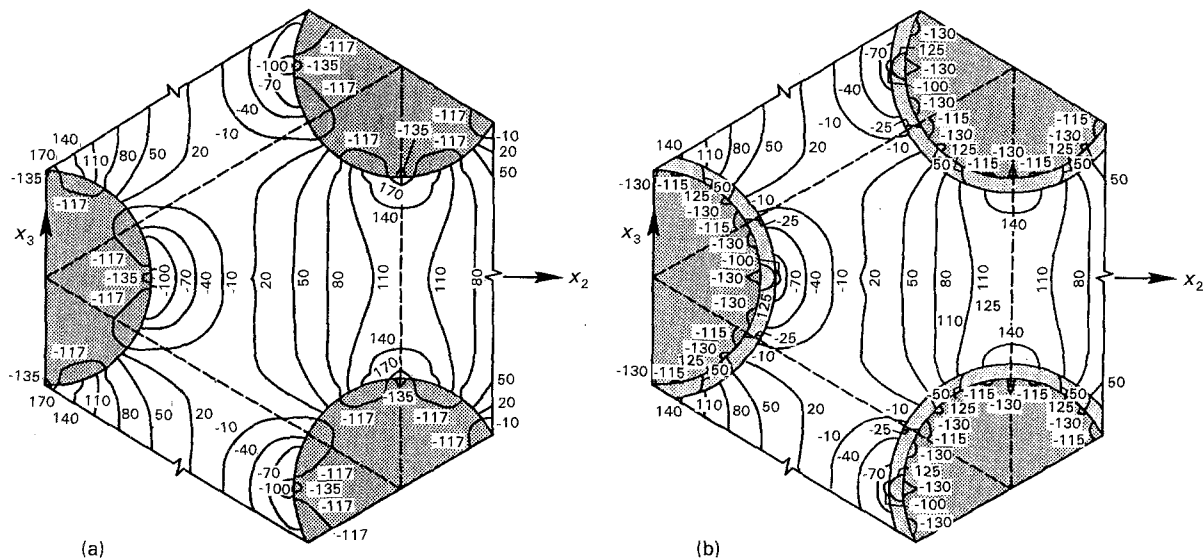
Figure 11 Transverse normal stresses, σ_{22}, in the SCS6/Ni$_3$Al composite after cooling from 1200 °C to room temperature: (a) uncoated fibre, (b) carbon-coated fibre.

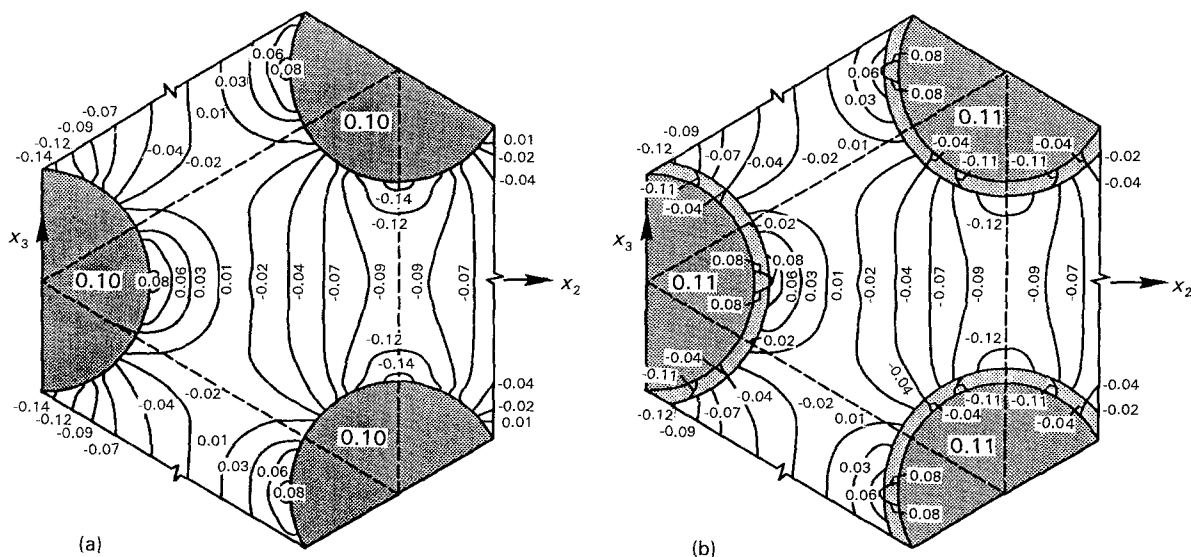*Figure 12* Transverse normal stresses in the SCS6/Ni$_3$Al composite from Fig. 11, normalized by $\Delta T = 1179$ °C: (a) uncoated fibre, (b) carbon-coated fibre.
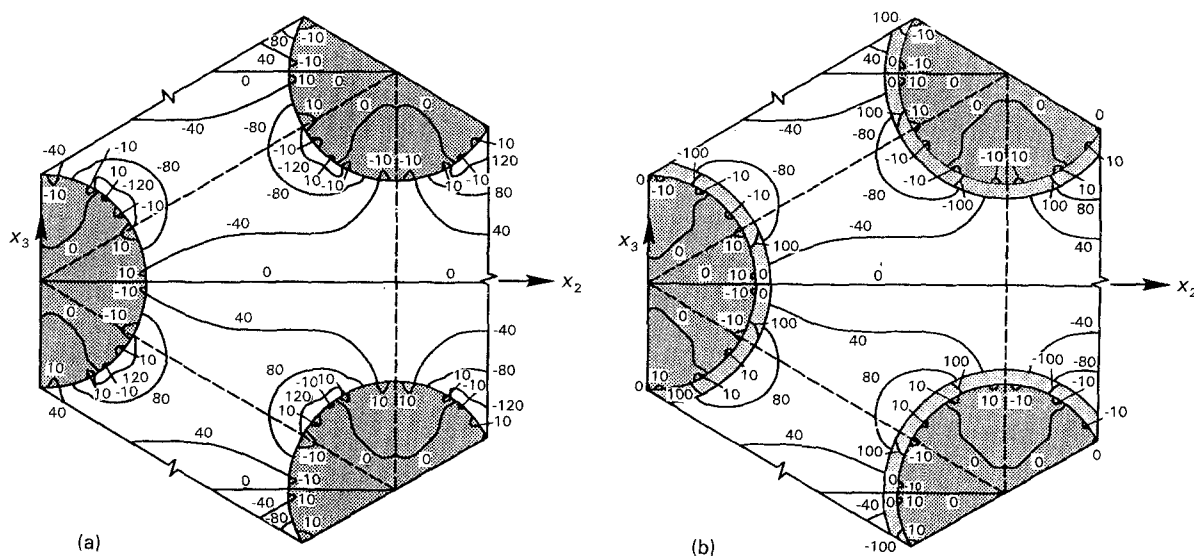

Figure 13 Shear stress, σ_{23}, in the tranverse plane of the SCS6/Ni$_3$Al composite after cooling from 1200 °C to room temperature: (a) uncoated fibre, (b) carbon-coated fibre.

the stiffness of the carbon coating so that the differences in the stress ratios found in the coated and the uncoated fibre systems are not significant. The deformation itself was quite extensive. For cooling from the assumed state free of internal stresses at 1200 °C, the onset of matrix yielding was found at 1140 °C, or after a −60 °C change in the uncoated fibre composite, and at 1020 °C, after a −180 °C change in the carbon-coated fibre system. Plastic yielding then proceeded along the entire cooling path to 21 °C.

Contours of the isotropic part of the local stress field are shown in Fig. 14, and of the normalized second invariant of the deviatoric stress field in Fig. 15. Large stress gradients are observed in the local fields. As expected, plastic flow of the matrix started at the fibre/matrix or coating/matrix interface where the stress concentrations were high. The stress contours indicate that the internal stresses can be approximated

by an axisymmetric field; this may not be possible at larger fibre concentrations. A comparison of Figs 14 and 15 indicates that the cooldown causes both large hydrostatic stresses and plastic flow in the entire matrix volume. Examples of evolution of plastic zones in the matrix during cooldown to room temperature are shown in Fig. 16.

Next, we turn our attention to the SCS6/Ti$_3$Al composite. Figs 17–20 illustrate the stresses found after cooling from 950 °C to room temperature. As indicated by the variation of the yield stress of the Ti$_3$Al matrix with temperature, Table III, the matrix remains mostly elastic in this case, Fig. 20. Consequently, relatively large stresses exist in the system after cooldown to room temperature. In the coated system, however, the stresses in the matrix are reduced by the compliant carbon coating and are similar to the stresses found in the nickel-based system.

Figure 14 Isotropic stress, σ$_0$, in the SCS6/Ni$_3$Al composite after cooling from 1200 °C to room temperature: (a) uncoated fibre, (b) carbon-coated fibre.

Figure 15 Effective stress $(3J_2)^{1/2}$ in the SCS6/Ni$_3$Al composite after cooling from 1200 °C to room temperature, normalized by y_m (21 °C) = 79 MPa, (a) uncoated fibre, (b) carbon-coated fibre.

10
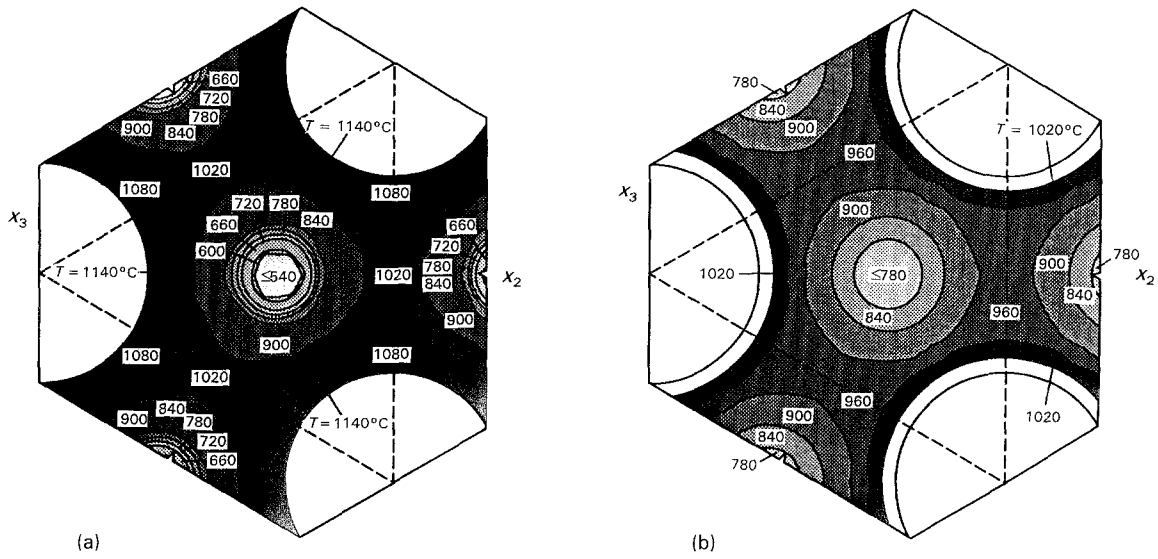
Figure 16 Evolution of plastic zones in the matrix SCS6/Ni$_3$Al composite during cooling from 1200 °C to room temperature: (a) uncoated fibre, (b) carbon-coated fibre.
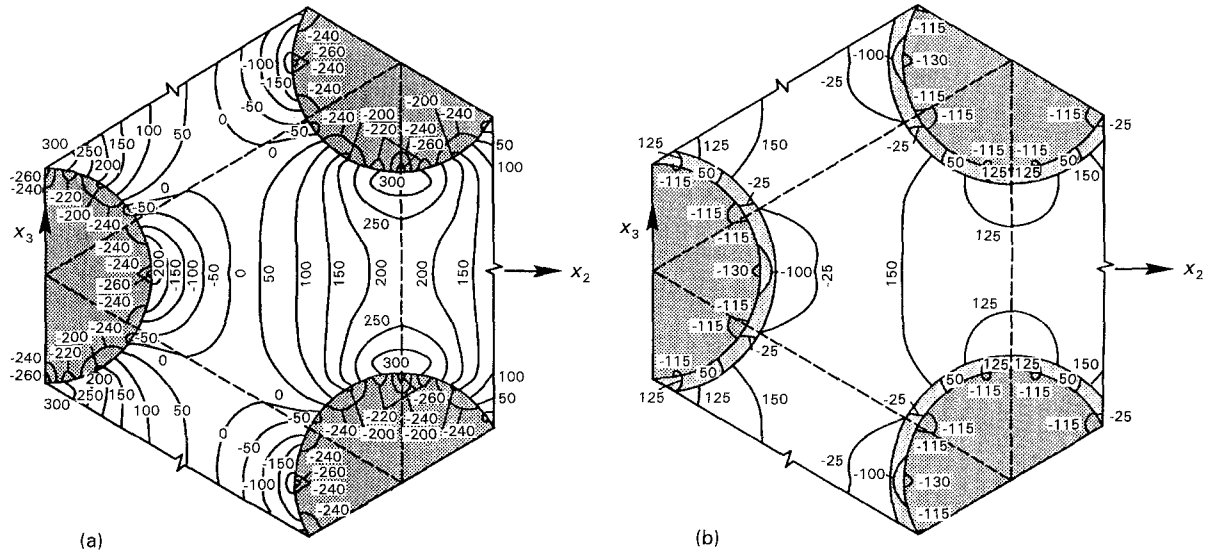
Figure 17 Transverse normal stresses, σ_{22}, in the SCS6/Ti$_3$Al composite after cooling from 950 °C to room temperature: (a) uncoated fibre, (b) carbon-coated fibre.
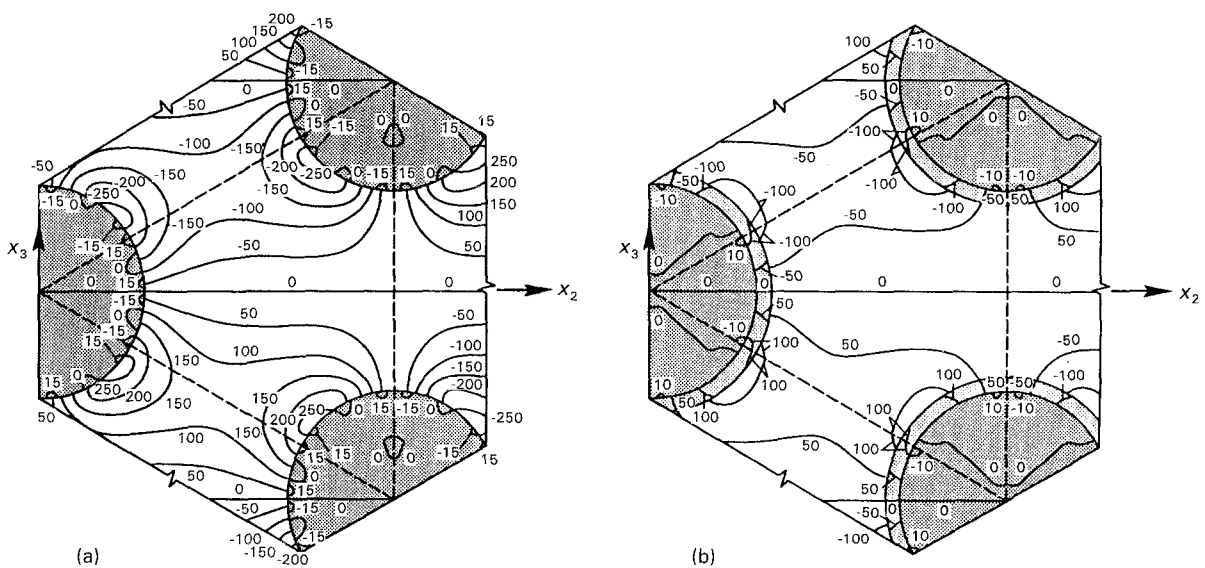
Figure 18 Shear stress, σ_{23}, in the tranverse plane of the SCS6/Ti$_3$Al composite after cooling from 950 °C to room temperature: (a) uncoated fibre, (b) carbon-coated fibre.
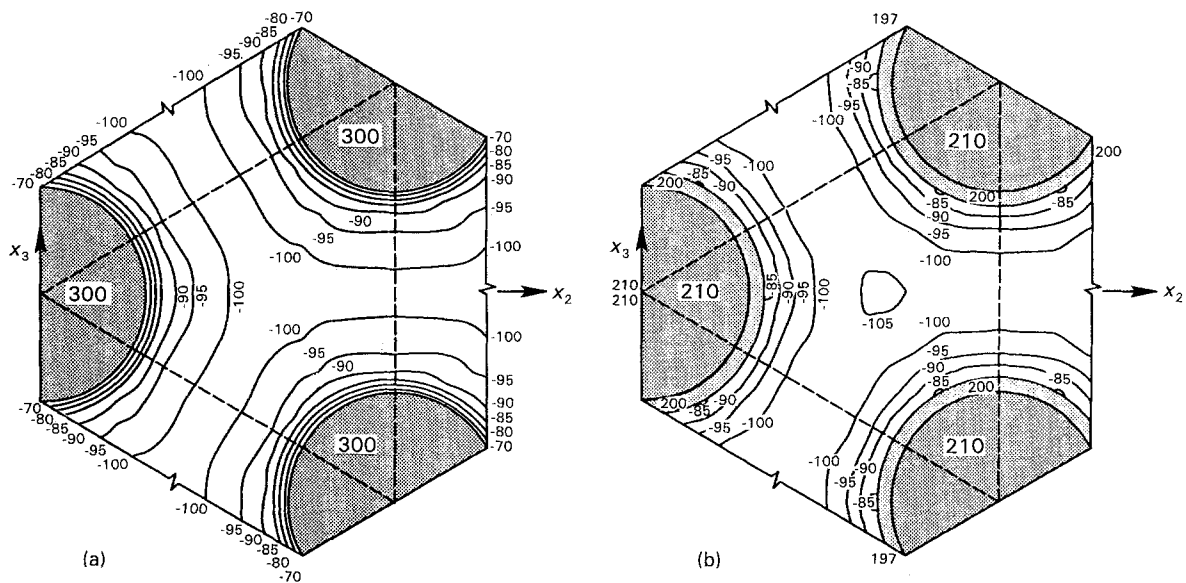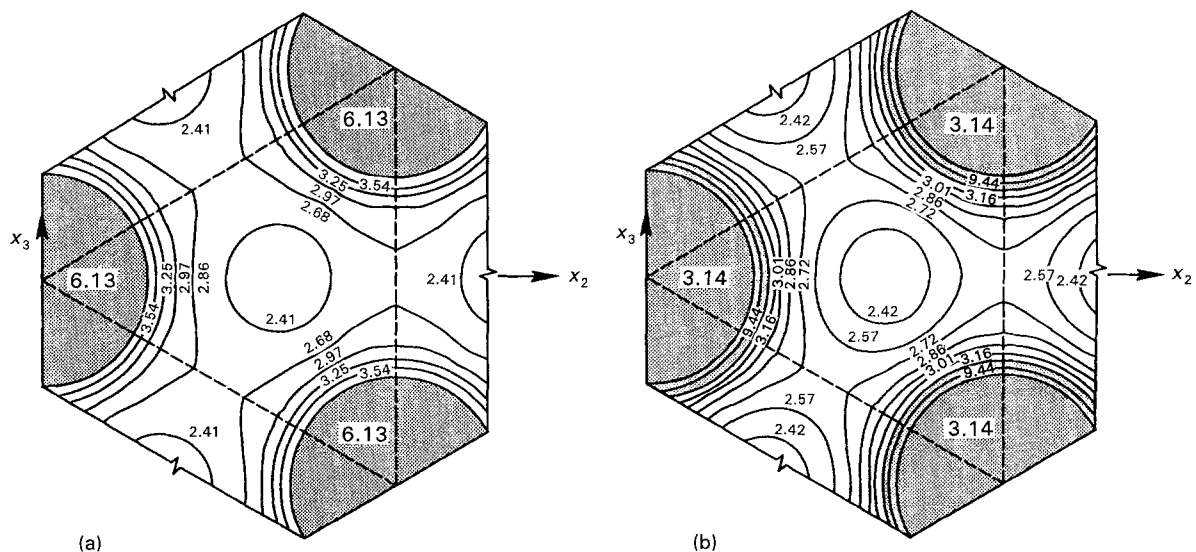
11
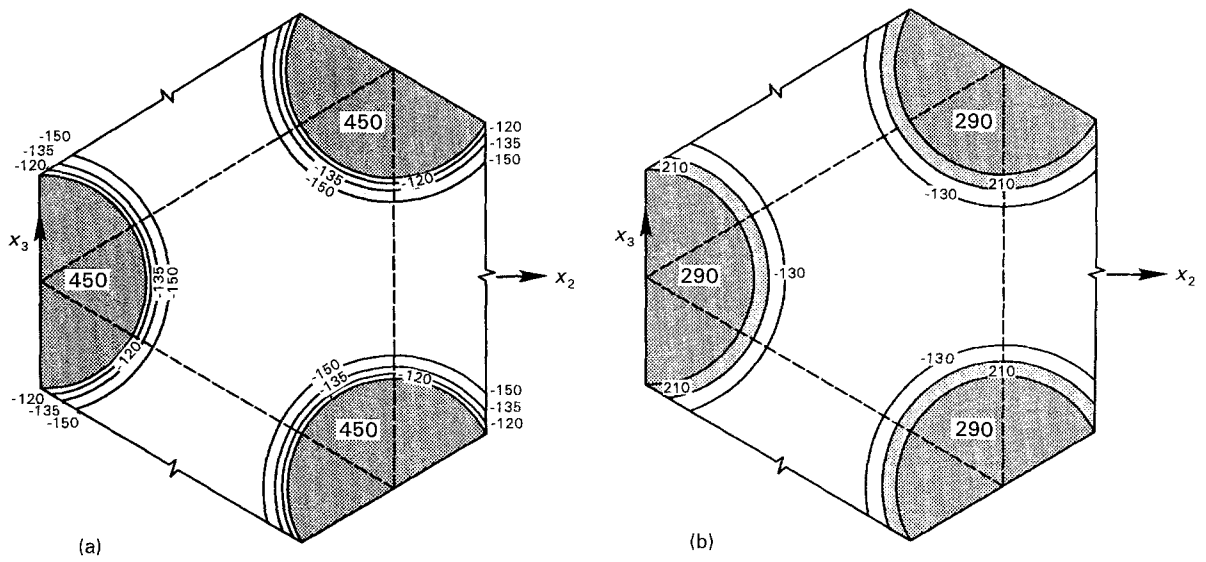
Figure 19 Isotropic stress, σ_0, in the SCS6/Ti$_3$Al composite after cooling from 950 °C to room temperature: (a) uncoated fibre, (b) carbon-coated fibre.

Figure 20 Effective stress, $(3J_2)^{1/2}$, in the SCS6/Ti$_3$Al composite after cooling from 950 °C to room temperature, normalized by y_m (21 °C) = 500 MPa (a) uncoated fibre, (b) carbon-coated fibre.
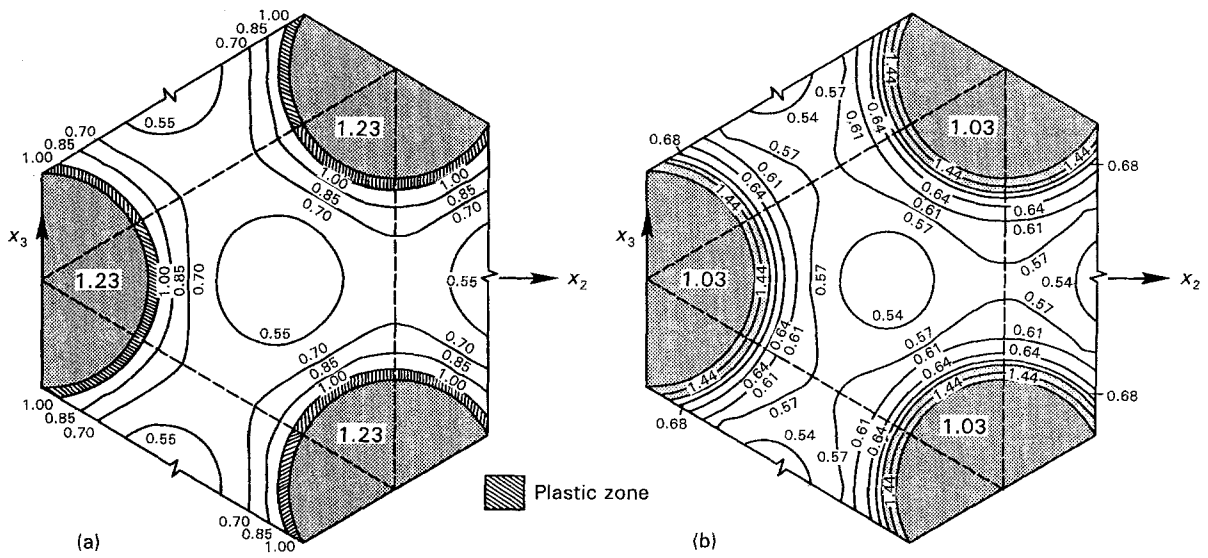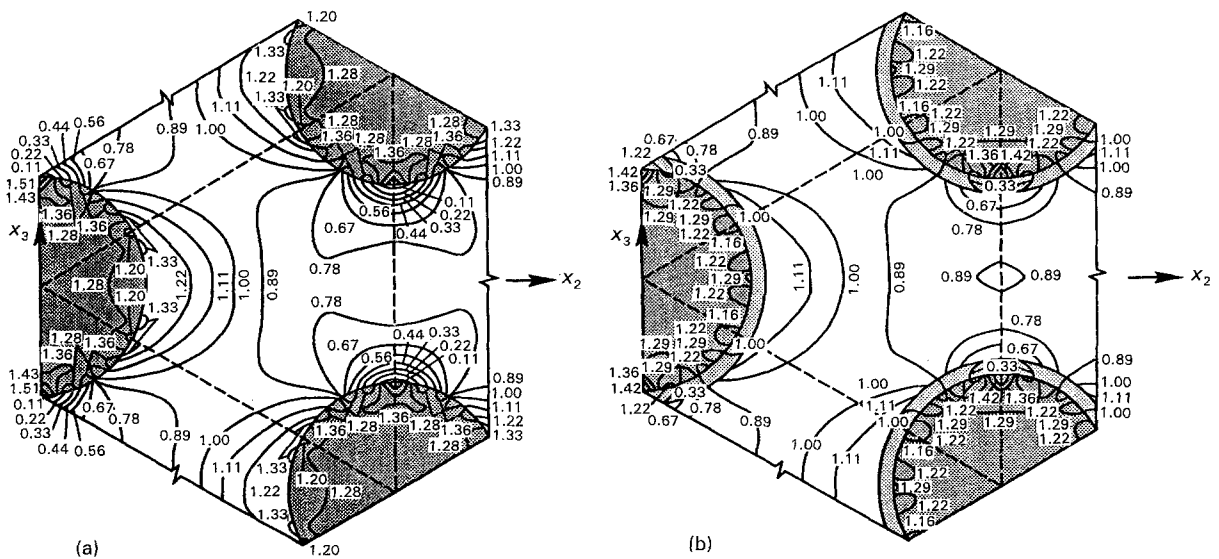

Figure 21 Normalized tranverse normal stresses, $\Delta\sigma_{22}/\Delta\bar{\sigma}_{22}$, in the SCS6/Ni$_3$Al composite after loading by overall transverse normal stress to $\bar{\sigma}_{22}$ = 225 MPa.
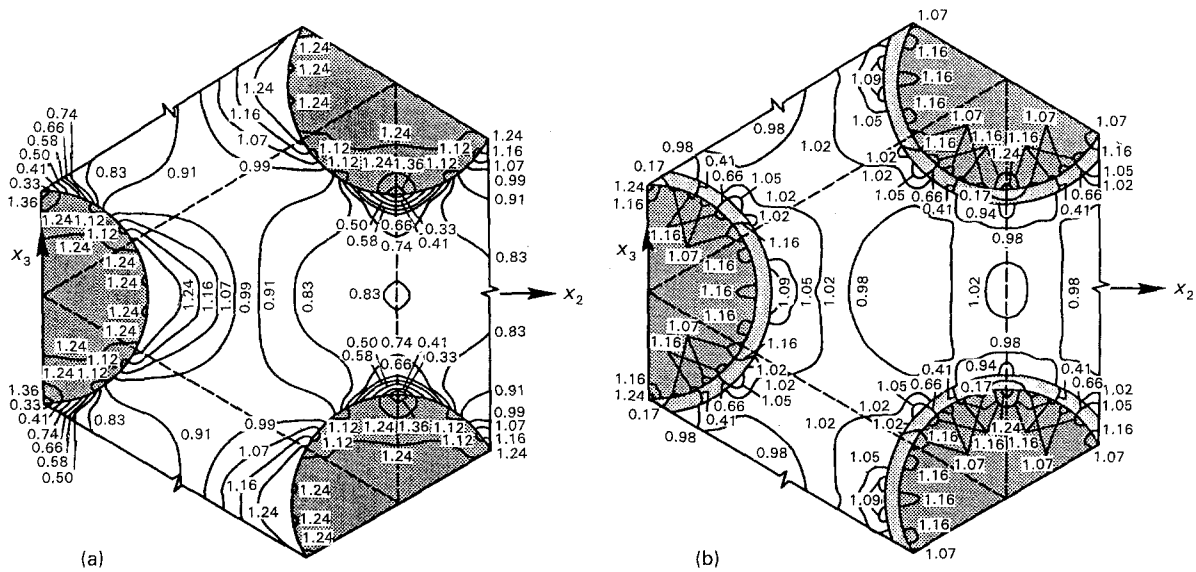
12

Figure 22 Normalized tranverse normal stresses, $\Delta\sigma_{22}/\Delta\bar{\sigma}_{22}$, in the SCS6/Ti$_3$Al composite after loading by overall transverse normal stress to $\bar{\sigma}_{22} = 605$ MPa.

To illustrate the magnitudes of local stresses caused during inelastic deformation under mechanical loading, we present results for loading from a stress-free state by an overall transverse tension stress to such levels that produced sustained plastic straining in all subelements in the matrix volume. These were found as $\bar{\sigma}_{22} = 225$ MPa in the SCS6/Ni$_3$Al and $\bar{\sigma}_{22} = 605$ MPa in the SCS6/Ti$_3$Al matrix systems. The local stresses computed in the two composite systems at these stress levels were normalized by the applied load and contours were plotted in the unit cell, Figs 21 and 22. Selected local stress ratios appear in Table IV.

The results indicate that material selection for monotonic loading should favour uncoated fibrous systems with ductile, compliant matrices over coated fibres systems with matrices which remain elastic or rather stiff during plastic flow. However, plastic straining should be avoided under cyclic loads as it may lead to low-cycle fatigue damage of the matrix.

5. Simulation of hot isostatic pressing
5.1. Analysis of the standard process
We now proceed to examine the stress states created in the two intermetallic composite systems by hot isostatic pressing (HIP). In addition to the standard pressure–temperature cycle, we explored pressure and temperature combinations that could lead to more favourable distribution of residual stresses after cooling to room temperature and reheating to the operating temperature. The results were obtained for the PHA domain shown in Fig. 3b using the ABAQUS finite element program. The composite was assumed to be free of external loads and internal stresses at the beginning of the path at fabrication temperature. Then, the selected pressure was applied in a single step if the composite remained elastic, or incrementally when plastic straining was involved. This was followed by combined pressure and temperature changes dur-

ing cooling. As in Section 2.2, a rate-independent thermoplasticity theory was used. The analysis neglects the role of possible rate effects, and thus implies that cooldown to room temperature and reduction of the hydrostatic stress to the atmospheric value take place at a very slow rate. Evaluation of the rate effects during fabrication, which may be significant in some composite systems, requires application of a viscoplasticity theory for the ductile phases. This has been considered in our yet unpublished work using the viscoplastic constitutive equations reported by Bahei-El-Din et al. [16] and Shah [26].

The temperature–overall hydrostatic pressure combinations applied to the SCS6/Ni$_3$Al composite are shown schematically in Fig. 23. Conditions similar to those shown in Fig. 23a and c were applied to the SCS6/Ti$_3$Al system; however, the fabrication temperature was taken as $T_0 = 950\,°C$, and the initial pressure as 200 or 400 MPa. In addition, we applied modified pressure conditions, with the ratio of the axial to transverse hydrostatic pressure ranging from 0–1.5, to promote plastic yielding of the matrix.

In typical HIP cycles, the cooling/unloading path to room temperature and atmospheric pressure is usually linear, as in Fig. 23a. Under the hydrostatic load, the local stress field is not necessarily isotropic, hence plastic flow may take place in the matrix during application of the pressure, σ_0. In the systems considered, the local stresses in the matrix are dominated by an isotropic stress field so that the matrix, which is assumed to be plastically incompressible, remains elastic at the fabrication temperature and 200 MPa hydrostatic pressure. However, the two intermetallic composites exhibited different deformation behaviour under the linear cooldown/depressurization cycle. In agreement with the variation of the yield stress with temperature of the nickle aluminide and the titanium aluminide matrix, Fig. 6, the SCS6/Ni$_3$Al composite exhibited substantial plastic deformations while the SCS6/Ti$_3$Al composite remained mainly elastic.

13
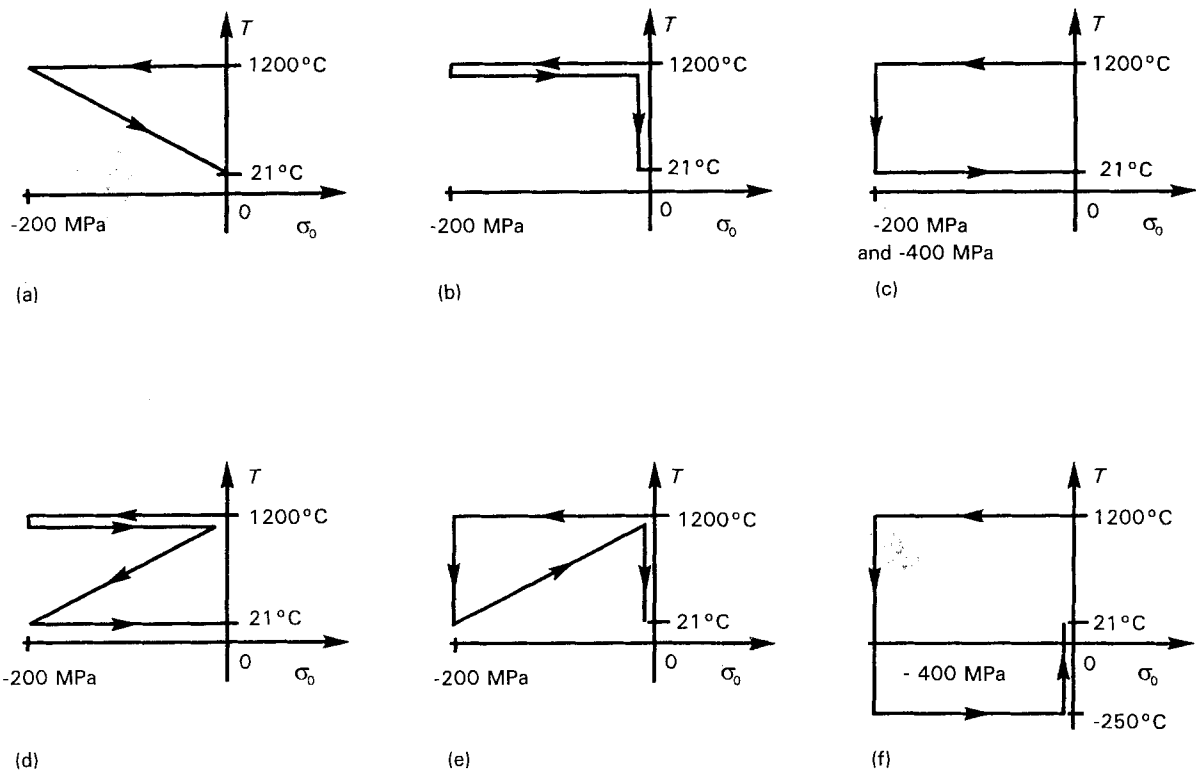
Figure 23 Thermomechanical unloading programmes applied to simulate modified hot isostatic pressing.

Fig. 24 shows the distribution of the axial, radial, and hoop stresses, $\sigma_{11} \equiv \sigma_{11}$, σ_{rr}, $\sigma_{\theta\theta}$, along the x_2-axis in the unit cell for uncoated and coated SCS6/Ni$_3$Al composite after the HIP cycle, at room temperature and in complete unloading. The inset in the figures indicates the loading/unloading path assumed in this simulation. The axial stress in the fibre is uniform and compressive. The magnitude of the fibre axial stress is reduced substantially if the fibre is coated by a thin carbon layer. However, the coating itself sustains large axial tensile stress after cooldown to room temperature. The matrix axial stress is also uniform, but the radial and hoop stresses are not uniform. Large tensile stresses develop in the matrix at
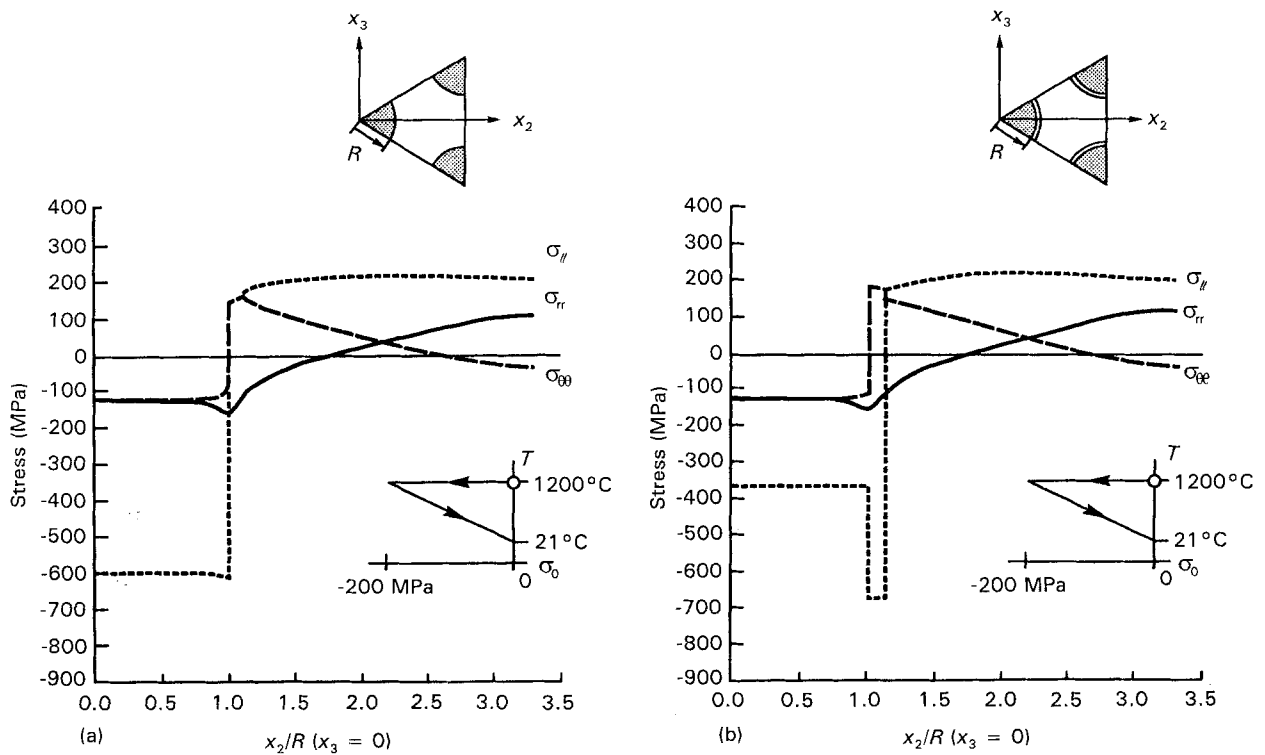
Figure 24 Distribution of axial, radial and hoop stresses in the SCS6/Ni$_3$Al composite at room temperature after hot isostatic pressing: (a) uncoated fibre, (b) carbon-coated fibre.

14

the fibre/matrix interface in the axial and hoop directions. Comparing the plots in Fig. 24a and b, we see that the matrix stress in the SCS6/Ni$_3$Al composite does not benefit from the presence of the fibre coating.

Fig. 25 shows the internal stresses after reheating to 1200 °C. Because the composite deformed plastically

in the cooling cycle, the residual stresses did not vanish after reheating.

Depending on the direction of the subsequent load, the residual stresses may improve or impair the overall strength. For example, if overall transverse tension is applied to the composite at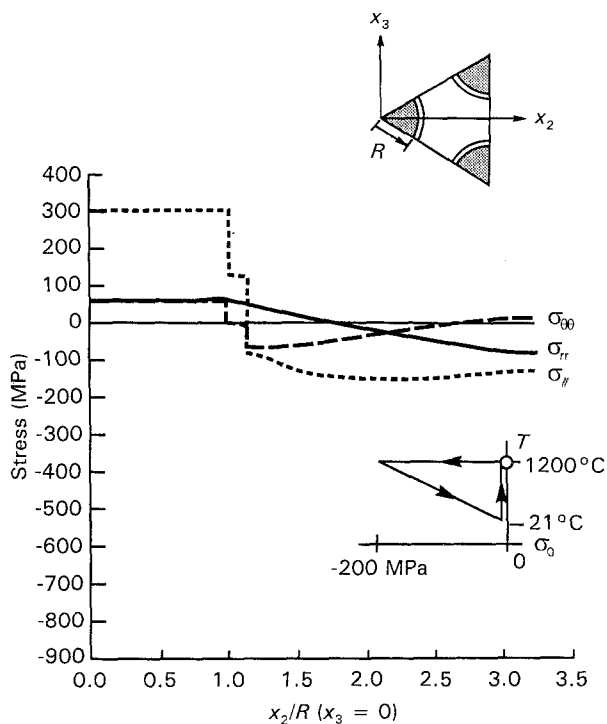 1200 °C (see the contours in Figs 9 and 12) the matrix tensile stress in the radial direction is elevated by the residual stress, whereas the tensile stress in the hoop direction is reduced by the compressive residual stress. This reduces the likelihood of developing radial cracks in the matrix and increases the possibility of debonding at the interface.

The residual stresses found at room temperature in uncoated and coated SCS6/Ti$_3$Al composite are shown in Fig. 26. Compared to the nickel-based system, much larger thermal stresses were found in the matrix of the uncoated titanium-based system. Of course, this is the consequence of plastic straining in the Ni$_3$Al matrix, and elastic deformation in the Ti$_3$Al matrix. However, for the same reason, the magnitude of the radial and hoop stresses in the Ti$_3$Al matrix were reduced by more than a factor of two by the fibre coating, Fig. 26, while remained unchanged in the Ni$_3$Al matrix, Fig. 24. Also, the residual stresses were completely removed by reheating the Ti$_3$Al matrix composite to 950 °C.

Figure 25 Distribution of axial, radial and hoop stresses in the SCS6/Ni$_3$Al composite after hot isostatic pressing and reheating to 1200 °C: (a) uncoated fibre, (b) carbon-coated fibre.

5.2. Effect of HIP parameters on residual stresses

The results presented in the preceding sections indicate that plastic flow of the matrix causes redistribution of the local stresses and reduction of the
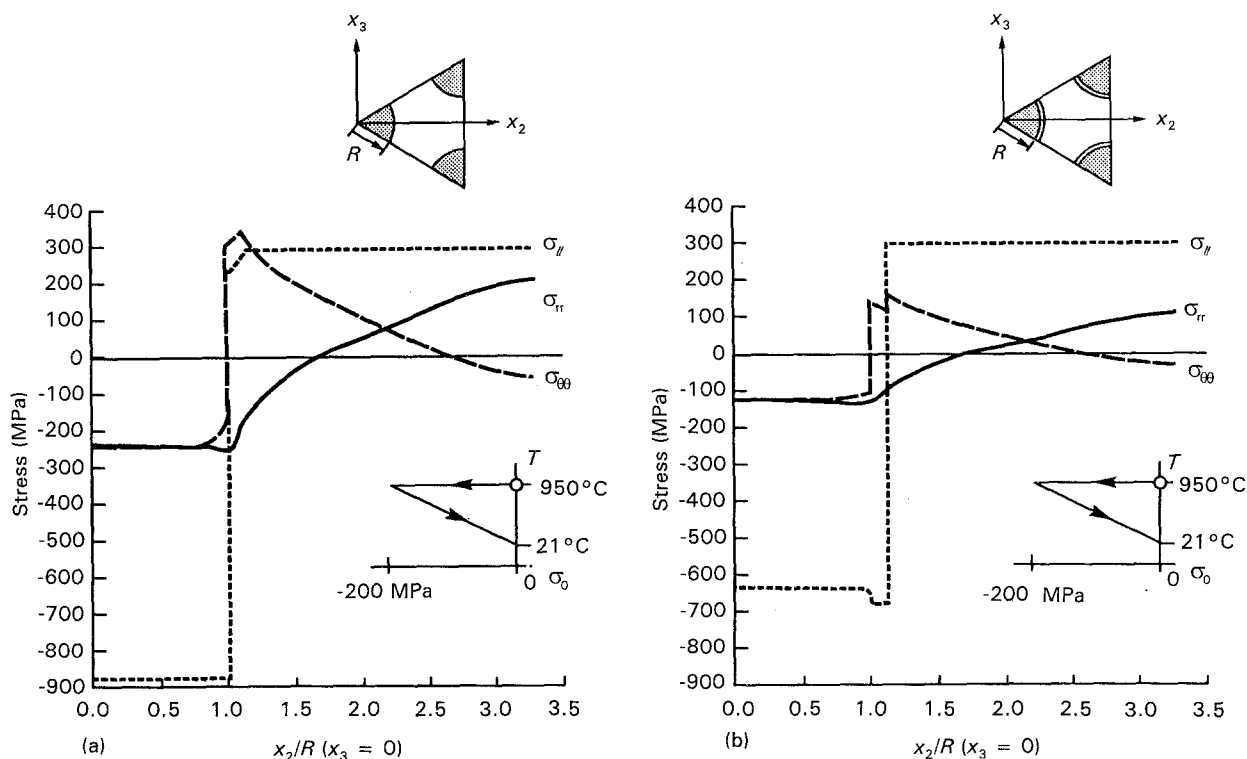

Figure 26 Distribution of axial, radial and hoop stresses in the SCS6/Ti$_3$Al composite at room temperature after hot isostatic pressing: (a) uncoated fibre, (b) carbon-coated fibre.

interfacial stresses in the matrix. This feature can be utilized in optimizing the temperature/pressure path in order to reduce the adverse local stresses. In this section, we examine various HIP regimes and evaluate the corresponding local stresses in the two intermetallic composites considered above.

First, we computed the local residual stresses retained in the SCS6/Ni$_3$Al system at room temperature after exposure to an HIP temperature of 1200 °C and hydrostatic pressure of 200 or 400 MPa, when unloading was reached through the various options shown in Fig. 23b–f, including an excursion below room temperature, Fig. 23f. For the loading cases shown in Fig. 23a, b, d and e, the stresses at the end of the HIP cycle were very similar. On the other hand, the tensile stresses were substantially reduced when the hydrostatic pressure, σ_0, was sustained during cooldown of the composite, Fig. 23c. Moreover, the tensile stresses in the phases were lower when the higher hydrostatic pressure of 400 MPa was maintained during the HIP process.

The interfacial and internal matrix stresses computed in uncoated and carbon-coated SCS6/Ni$_3$Al composites for the various conditions are shown in Tables V and VI. Table V lists the radial stress σ_{rr}, hoop stress $\sigma_{\theta\theta}$, and axial stress σ_{11}, found at the interface at either point "a" or point "b" indicated on

the unit cell shown in the inset. The average isotropic stress in the matrix σ_0^m is also indicated. Table VI shows the local stresses found in the matrix internal point "c" (see inset of unit cell), the axial stress $\sigma_{11}^m \equiv \sigma_{ll}$, the transverse stress σ_{22}^m and the isotropic stress σ_0^m.

Note the substantial reduction of the radial and hoop stresses at the interface between the first and last regimes in Tables V and VI. As discussed below, this reduction is mostly due to more extensive plastic straining caused by the higher and sustained hydrostatic stress. It appears that the tensile stresses would be reduced further by increasing the hydrostatic pressure, provided that fibre splitting could be avoided. The matrix interfacial tensile stresses in the coated system have been also reduced, but to a lesser extent, by following the loading path indicated in Fig. 23c, Table V. The hoop stress in the coating, however, is not affected by the thermomechanical path. The pressure applied during the HIP process did not much affect the stresses, in the coated system.

Of course, reheating to 1200 °C did not eliminate the residual stresses, Tables VII and VIII. However, the stresses in the reheated systems were not much affected by the processing path, or by the magnitude of the hydrostatic pressure, σ_0, applied.

Table IX summarizes the results found for the

TABLE V Maximum interface stresses found in a SCS6/Ni$_3$Al composite at room temperature after HIP

Interface stress (MPa)	Uncoated fibre	Coated fibre	Uncoated fibre	Coated fibre	Uncoated fibre	Coated fibre	Uncoated fibre	Coated fibre
σ_{rr}^m	− 98 at b	− 84 at b	− 79 at b	− 94 at b	− 60 at b	− 91 at b	− 34 at b	− 80 at b
$\sigma_{\theta\theta}^m$	190 at b	158 at b	155 at b	152 at b	120 at b	152 at b	127 at b	139 at b
σ_{11}^m	198 at b	186 at b	179 at b	143 at b	161 at b	141 at b	153 at b	123 at b
$\sigma_{\theta\theta}^c$	–	185 at a	–	188 at a	–	188 at a	–	198 at a
σ_{11}^c	–	− 668 at b	–	− 633 at b	–	− 624 at b	–	− 623 at b
σ_{rr}^f	− 98 at b	− 110 at b	− 79 at b	− 122 at b	− 60 at b	− 121 at b	− 34 at b	− 108 at b
$\sigma_{\theta\theta}^f$	− 94 at a	− 108 at a	− 76 at a	− 117 at a	− 59 at a	− 116 at a	− 39 at a	− 104 at a
σ_{11}^f	− 605 at b	− 364 at b	− 552 at b	− 280 at b	− 500 at b	− 261 at b	− 397 at b	− 186 at b
σ_0^m	97 at b	87 at b	85 at b	67 at b	74 at b	67 at b	82 at b	61 at b

TABLE VI Matrix internal stresses found in a SCS6/Ni$_3$Al composite at room temperature after HIP

Stress at point c (MPa)	Uncoated fibre	Coated fibre	Uncoated fibre	Coated fibre	Uncoated fibre	Coated fibre	Uncoated fibre	Coated fibre
$\sigma_{11}^m = \sigma_{ll}^m$	213	213	195	179	177	177	138	149
σ_{22}^m	115	128	96	162	76	164	42	141
σ_0^m	101	105	90	106	79	106	57	89

TABLE VII Maximum interface stresses found in a $SCS6/Ni_3Al$ composite at room temperature after HIP and reheating to fabrication temperature

Interface stress (MPa)	Uncoated fibre	Coated fibre	Uncoated fibre	Coated fibre	Uncoated fibre	Coated fibre	Uncoated fibre	Coated fibre
σ_{rr}^m	76 at a	52 at·a	76 at a	50 at a	76 at a	49 at a	77 at a	51 at a
$\sigma_{\theta\theta}^m$	−55 at a	−67 at a or b	−55 at a	−66 at b	−55 at a	−66 at b	−55 at a	−67 at a or b
σ_{ll}^m	−62 at a	−80 at a	−62 at a	−80 at a	−62 at a	−81 at a	−62 at a	−80 at a
$\sigma_{\theta\theta}^c$	−	7 at b	−	6 at b	−	6 at b	−	8 at b
σ_{ll}^c	−	126 at a or b	−	126 at a or b	−	126 at a or b	−	126 at a or b
σ_{rr}^f	76 at a	65 at a	76 at a	64 at a	76 at a	63 at a	77 at a	64 at a
$\sigma_{\theta\theta}^f$	72 at b	60 at b	72 at b	57 at b	72 at b	57 at b	71 at b	58 at b
σ_{ll}^f	372 at a	298 at a	372 at a	299 at a	373 at a	299 at a	373 at a	298 at a
σ_0^m	−14 at a	−32 at a	−14 at a	−33 at a	−14 at a	−34 at a	−13 at a	−32 at a

TABLE VIII Matrix internal stresses found in a $SCS6/Ni_3Al$ composite at room temperature after HIP and reheating to fabrication temperature

Stress at point c (MPa)	Uncoated fibre	Coated fibre	Uncoated fibre	Coated fibre	Uncoated fibre	Coated fibre	Uncoated fibre	Coated fibre
$\sigma_{11}^m = \sigma_{ll}^m$	−132	−127	−132	−124	−132	−123	−132	−124
σ_{22}^m	13	13	13	14	13	15	13	14
σ_0^m	−62	−64	−62	−63	−62	−62	−62	−63

TABLE IX Maximum interface stresses found in a $SCS6/Ti_3Al$ composite at room temperature after HIP

Interface stress (MPa)	Uncoated fibre	Coated fibre	Uncoated fibre	Coated fibre
σ_{rr}^m	−210 at b	−79 at a	−178 at b	−79 at a
$\sigma_{\theta\theta}^m$	323 at b	171 at a	165 at b	171 at a
σ_{ll}^m	253 at b	308 at a	133 at b	308 at a
$\sigma_{\theta\theta}^c$	−	146 at b	−	146 at b
σ_{ll}^c	−	−669 at b	−	−669 at b
σ_{rr}^f	−210 at b	−105 at b	−178 at b	−105 at b
$\sigma_{\theta\theta}^f$	−182 at a	−106 at a	−149 at a	−105 at a
σ_{ll}^f	−883 at b	−632 at b	−827 at b	−632 at b

uncoated and carbon-coated $SCS6/Ti_3Al$ composites. Apart from very localized matrix yielding at the fibre/matrix interface in the uncoated fibre system, this composite remained elastic when subjected to the loading path indicated in Fig. 23a at 950 °C. The matrix also remained elastic and the local stresses were unaltered when the hydrostatic pressure, σ_0, was increased from 200 MPa to 400 MPa and then
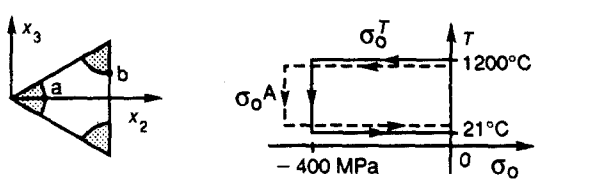
reduced proportionally during cooling. On the other hand, plastic flow of the matrix was induced early in the HIP process of the uncoated fibre system, and the matrix experienced substantial plastic deformation when the HIP path shown in Fig. 23c was followed from 950 °C at sustained hydrostatic pressure of 400 MPa. The hoop stress and the axial stress in the matrix of the uncoated system were reduced by approximately 49%. These reductions in the local stresses are larger than those found in the nickel-based system, Table V. This may be attributed to more extensive plastic straining at the low plastic tangent modulus of the titanium aluminide matrix, Table III.

5.3. Modified pressure ratios

To explore other possible alternatives that could magnify the favourable effect of plastic straining on the distribution of residual stresses, we applied modified HIP cycles in which the axial pressure σ_0^A, and the transverse hydrostatic pressure σ_0^T, assumed different magnitudes. The results are shown in Tables X–XIII for $\sigma_0^T = 400$ MPa, and σ_0^A/σ_0^T ratios of 0.0, 0.5, 1.0, 1.5. In these calculations, the axial pressure and the transverse hydrostatic pressure were held constant during cooldown to room temperature.
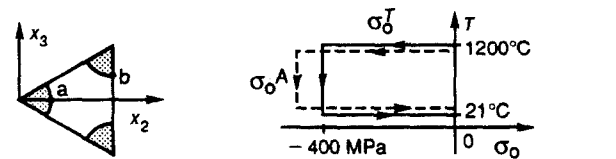
The axial tensile stress in the matrix benefited most from reducing the axial pressure during hot isostatic pressing of the composite, particularly in uncoated fibre systems. Compared to the standard HIP methods in which a three-dimensional hydrostatic pressure was applied, $\sigma_0^A = \sigma_0^T$, the matrix axial stress was reduced by 50%–60% in the SCS6/Ni$_3$Al composite when $\sigma_0^A/\sigma_0^T = 0.5$, and by 73%–115% in the SCS6/Ti$_3$Al composite when $\sigma_0^A/\sigma_0^T = 0.0$. As expected, the axial compressive stress in the fibre and

TABLE X Interface stresses found in uncoated SCS6/Ni$_3$Al composite at room temperature after HIP with modified pressure conditions
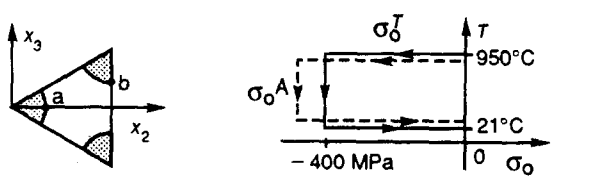

Interface stress (MPa)	σ_0^A/σ_0^T			
	0.0	0.5	1.0	1.5
σ_{rr}^m at a	− 100	− 106	− 107	− 109
at b	− 61	− 62	− 59	− 66
$\sigma_{\theta\theta}^m$ at a	110	102	88	117
at b	131	129	120	142
σ_{11}^m at a	55	49	125	191
at b	79	78	162	221
$\sigma_{\theta\theta}^f$ at a	− 57	− 59	− 58	− 62
at b	− 86	− 89	− 88	− 93
σ_{11}^f at a	− 194	− 196	− 508	− 612
at b	− 188	− 190	− 501	− 606

TABLE XI Interface stresses found in carbon-coated SCS6/Ni$_3$Al composite at room temperature after HIP with modified pressure conditions

Interface stress (MPa)	σ_0^A/σ_0^T			
	0.0	0.5	1.0	1.5
σ_{rr}^m at a	− 98	− 108	− 113	− 107
at b	− 86	− 90	− 91	− 92
$\sigma_{\theta\theta}^m$ at a	149	149	150	150
at b	156	156	152	154
σ_{11}^m at a	112	121	134	149
at b	109	125	141	163
$\sigma_{\theta\theta}^c$ at a	160	163	166	163
at b	162	159	155	159
σ_{11}^c at a	− 571	− 592	− 630	− 654
at b	− 565	− 586	− 625	− 649
σ_{rr}^f at a	− 154	− 165	− 170	− 165
at b	− 112	− 118	− 121	− 120
$\sigma_{\theta\theta}^f$ at a	− 107	− 114	− 116	− 115
at b	− 144	− 154	− 161	− 155
σ_{11}^f at a	− 126	− 176	− 270	− 327
at b	− 121	− 170	− 265	− 322

TABLE XII Interface stresses found in uncoated SCS6/Ti$_3$Al composite at room temperature after HIP with modified pressure conditions
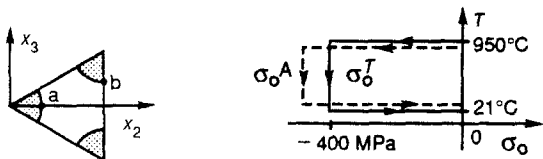

Interface stress (MPa)	σ_0^A/σ_0^T			
	0.0	0.5	1.0	1.5
σ_{rr}^m at a	− 174	− 190	− 204	− 210
at b	144	− 161	− 178	− 190
$\sigma_{\theta\theta}^m$ at a	141	139	135	141
at b	168	167	165	168
σ_{11}^m at a	− 13	37	90	148
at b	35	85	133	182
$\sigma_{\theta\theta}^f$ at a	− 119	− 132	− 149	− 156
at b	− 184	− 205	− 219	− 229
σ_{11}^f at a	− 530	− 736	− 815	− 841
at b	− 538	− 748	− 827	− 855

coating was lower when the overall axial pressure was reduced.

In contrast, the tensile matrix hoop stress found in all cases considered in Tables X–XIII changed only slightly when the overall axial pressure and the transverse hydrostatic pressure had different magnitudes $\sigma_0^A \neq \sigma_0^T$.

TABLE XIII Interface stresses found in carbon-coated SCS6/Ti$_3$Al composite at room temperature after HIP with modified pressure conditions

Interface stress (MPa)	σ_0^A/σ_0^T			
	0.0	0.5	1.0	1.5
σ_{rr}^m at a	− 93	− 83	− 79	− 79
at b	− 101	− 89	− 84	− 84
$\sigma_{\theta\theta}^m$ at a	208	189	171	171
at b	194	177	165	165
σ_{11}^m at a	211	271	308	308
at b	221	289	304	304
$\sigma_{\theta\theta}^c$ at a	127	128	130	130
at b	126	126	125	125
σ_{11}^c at a	− 584	− 653	− 669	− 669
at b	− 586	− 655	− 671	− 671
σ_{rr}^f at a	− 159	− 145	− 139	− 139
at b	− 123	− 110	− 105	− 105
$\sigma_{\theta\theta}^f$ at a	− 123	− 110	− 105	− 105
at b	− 148	− 134	− 128	− 128
σ_{11}^f at a	− 434	− 601	− 640	− 640
at b	− 427	− 593	− 632	− 632

5.4. Mechanical loading of processed composites

To complete the numerical simulations of the inelastic response of the two composite systems, we applied transverse tension stresses to systems processed with the standard and modified HIP cycles. The mechanical stress levels chosen were equal to those employed earlier to stress-free systems in Figs 21 and 22. The processing sequences and local stress magnitudes at the maximum stress are shown in Tables XIV and XV. Then, Table XVI compares the local stresses attained after fabrication alone, following the regime indicated in the table, with those found after mechanical loading applied alone from a stress-free state at room temperature (Section 4.2) and finally with those found after transverse loading of the fabricated composites with the initial residual stresses.
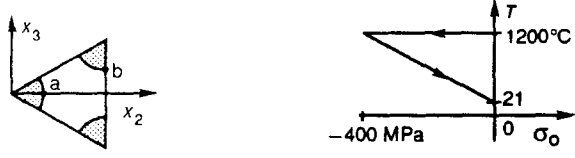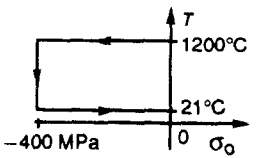
Note that during plastic straining of the fabricated systems, the differences in the residual stresses after fabrication, Tables V and VI, have no discernible effect on the final stress state. However, there are large differences between the local stresses reached after loading from the stress-free state, and from the fabricated state.

5.5. Interpretation of the results

To gain a better insight into the numerical results, we present here a simplified analysis of unidirectional fibrous systems exposed to pressure/temperature loads, using the thermomechanical equivalence [34, 35]. The local fields and overall response under thermal changes applied to elastic or inelastic, unidirectionally reinforced fibrous composites can be found by superposition of a certain uniform stress field in the phases with a field corresponding to an overall mechanical load that removes the surface tractions of the uniform stress field.
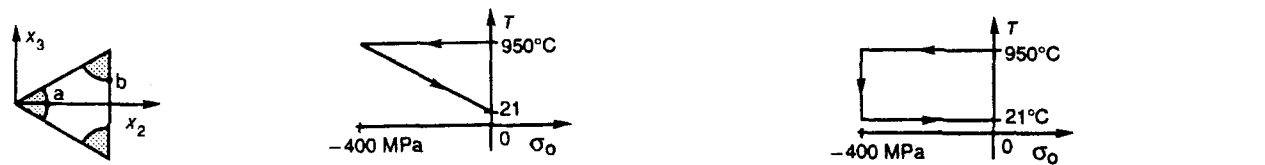
For composites with two isotropic phases of any microgeometry, which are subjected to a uniform

TABLE XIV Interface stress found in SCS6/Ni$_3$Al composite at room temperature after HIP and transverse tension of 255 MPa
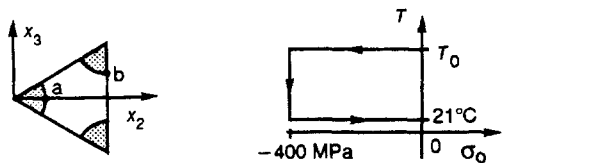

Interface stress (MPa)	$+ \bar\sigma_{22} = 225$ MPa		$+ \bar\sigma_{22} = 225$ MPa	
	Uncoated fibre	Coated fibre	Uncoated fibre	Coated fibre
σ_{rr}^m at a	170	192	171	191
at b	− 143	− 135	− 143	− 135
$\sigma_{\theta\theta}^m$ at a	311	249	310	251
at b	170	245	169	245
σ_{11}^m at a	322	310	320	311
at b	104	157	99	157
$\sigma_{\theta\theta}^c$ at a	–	128	–	126
at b	–	226	–	227
σ_{11}^c at a	–	− 674	–	− 674
at b	–	− 738	–	− 737
σ_{rr}^f at a	170	184	171	183
at b	− 143	− 125	− 143	− 125
$\sigma_{\theta\theta}^f$ at a	− 51	− 52	− 49	− 52
at b	257	230	259	230
σ_{11}^f at a	− 686	− 432	− 684	− 432
at b	− 680	− 439	− 678	− 438

TABLE XV Interface stresses found in SCS6/Ti$_3$Al composite at room temperature after HIP with transverse tension of 605 MPa

Interface stress (MPa)	+ σ̄$_{22}$ = 605 MPa		+ σ̄$_{22}$ = 605 MPa	
	Uncoated fibre	Coated fibre	Uncoated fibre	Coated fibre
σ$^m_{rr}$ at a	578	593	626	593
at b	75	− 53	68	− 53
σ$^m_{θθ}$ at a	500	53	348	53
at b	511	604	418	604
σ$^m_{11}$ at a	454	408	323	408
at b	253	287	160	287
σ$^c_{θθ}$ at a	–	24	–	24
at b	–	244	–	244
σ$^c_{11}$ at a	–	− 662	–	− 662
at b	–	− 787	–	− 787
σ$^f_{rr}$ at a	578	664	626	664
at b	75	7	68	7
σ$^f_{θθ}$ at a	− 165	41	− 74	42
at b	702	762	735	762
σ$^f_{11}$ at a	− 1076	− 733	− 1009	− 733
at b	− 1005	− 721	− 972	− 721

TABLE XVI Comparison of matrix interface stresses found in intermetallic matrix composites after fabrication and transverse tension

Interface stress (MPa)	SCS6/Ni$_3$Al		SCS6/Ti$_3$Al	
	Uncoated fibre	Coated fibre	Uncoated fibre	Coated fibre
Fabrication	T_0 = 1200 °C		T_0 = 950 °C	
σ$_{rr}$ at a	− 107	− 113	− 204	− 79
σ$_{θθ}$ at b	120	152	165	165
Overall σ̄$_{22}$	225 MPa		605 MPa	
σ$_{rr}$ at a	277	250	774	629
σ$_{θθ}$ at b	25	126	206	563
	Fab. + 225 MPa		Fab. + 605 MPa	
σ$_{rr}$ at a	171	191	626	593
σ$_{θθ}$ at b	169	245	418	604

temperature change $(T - T_0)$, one can find the uniform stress field in phases as

$$S = - [3(\alpha_f - \alpha_m)/(1/K_f - 1/K_m)](T - T_0) \quad (14)$$

where the elastic bulk modulus and coefficient of thermal expansion of the matrix and fibre are denoted, respectively, by K_m, α_m, K_f, α_f.

If thermoelastic properties of the phases are functions of temperature, then K_m and K_f denote the magnitudes of the phase bulk moduli at the current temperature T, whereas α_m and α_f are replaced by the averages $\{\int_{T_0}^{T} \alpha_r(T)dT\}/(T - T_0)$, $r = f, m$ [36]. In typical composite systems with isotropic phases in which

$K_f > K_m$ and $\alpha_f < \alpha_m$, the cooldown from T_0 to T causes uniform hydrostatic tension, Equation 14, in the entire composite. Because S is an isotropic stress in all phases, it does not cause inelastic deformation in a plastically incompressible material.

Of course, the internal field S is supported by corresponding surface tractions which are not actually applied at the surface of the representative volume, and must, therefore, be removed. If an overall uniform stress, σ̄, is applied to the composite simultaneously with the temperature change, then the corresponding tractions can be added to those created by an overall stress equal to $-S$. The local stress $\sigma(x)$ referred to a Cartesian coordinate system, x_j, $j = 1, 2, 3$, is then given by [34, 37]

$$\sigma(x) = S1 + B(x)(\bar{\sigma} - S1) \quad (15)$$

where $1 = [1\,1\,1\,0\,0\,0]^T$, and $B(x)$ is a (6×6) stress concentration factor matrix. Note that this stress is not uniform and may cause yielding. For fibrous media with transversely isotropic phases, where x_1 is the fibre axial direction, the matrix B has the form [35]

$$B = \begin{bmatrix} B_{11} & B_{12} & B_{12} & 0 & 0 & 0 \\ B_{21} & B_{22} & B_{23} & 0 & 0 & 0 \\ B_{21} & B_{23} & B_{22} & 0 & 0 & 0 \\ 0 & 0 & 0 & B_{44} & 0 & 0 \\ 0 & 0 & 0 & 0 & B_{55} & 0 \\ 0 & 0 & 0 & 0 & 0 & B_{55} \end{bmatrix} \quad (16)$$

The respective columns of B represent the local stresses corresponding to a sequence of unit overall stresses σ = i_k, $k = 1, 2, ..., 6$, where i_k is the kth column of a (6×6) unit matrix. Actual magnitudes of the coefficients must be found from analysis of a selected micromechanical model. Such models typically

approximate the actual fields with piecewise uniform distributions in a representative volume of the composite. The periodic hexagonal array (PHA) model [8, 9] employed here is an example of this approach. Other examples are the self-consistent method [1], Mori–Tanaka model [2, 3], and the vanishing fibre diameter model [38], in which only the phase average stresses are determined. Hence, if N denotes the number of subelements, one finds $N = 2$ for the averaging models of two-phase composites, and N equal to the number of subelements or integration points in the unit cell of the PHA model. In any case, Equation 15 is replaced by

$$\sigma_r = S1 + B_r(\bar{\sigma} - S1), \quad r = 1, 2, ..., N \quad (17)$$

Under hot isostatic pressing of unidirectional composites, the applied overall stress is usually the three-dimensional hydrostatic stress, σ_0. Substituting $\bar{\sigma} = \sigma_0 1$ in Equation 17, the local stresses caused by the thermomechanical loading are given by

$$\sigma_r = S1 + B_r S^* 1, \quad S^* = (\sigma_0 - S), \quad r = 1, 2, ..., N \quad (18)$$

In this way, the thermomechanical HIP problem is reduced to a mechanical problem in which the composite is subjected to hydrostatic pressure $(\sigma_0 - S)$. Note that S^* is often negative.

In modelling of the hot isostatic pressing of SCS6/Ni$_3$Al and SCS6/Ti$_3$Al composites reinforced by uncoated fibres, the cooldown part of the thermomechanical loading regimes shown in Fig. 23 was converted into the stress S, using Equation 14 and the thermoelastic properties listed in Tables I–III. This stress was combined with the hydrostatic pressure, σ_0, applied in the HIP process, and plotted against the

current temperature. The individual points were connected by straight line segments. The hydrostatic pressure path found in this manner for selected HIP loading regimes is shown in Figs 27 and 28 for SCS6/Ni$_3$Al and SCS6/Ti$_3$Al composites, respectively. The non-linear variation of this normalized pressure with temperature is caused, in part, by the temperature dependence of the yield stress and thermoelastic properties of the phases.

This replacement of the actual thermomechanical loads by the pressure $S^* = (\sigma_0 - S)$ simplifies evaluation of the onset of initial yielding of the composite under standard and modified HIP regimes. The magnitude of the overall hydrostatic stress, S_Y^*, at initial yielding in the matrix is found by substituting the local stresses given by Equation 18 into a specified yield function. Of course, N such solutions can be found, but only the lowest S_Y^* corresponds to the onset of yielding. In a J_2 material, the local hydrostatic stress given by the first term in Equation 18 causes no plastic deformation. Using the local stresses given by the second term in Equation 18, and adopting the Mises yield function (Equation 7) for the matrix material, one finds the overall hydrostatic stress at initial yielding as

$$S_Y^{*r} = Y/(B_{11}^r + 2B_{12}^r - B_{21}^r - B_{22}^r - B_{23}^r), \quad r = 1, N \quad (19)$$

In the self-consistent method, Equation 19 provides a single solution. This is indicated by the upper dashed curve in Figs 27 and 28. Under the HIP loads shown, the onset of yielding is given by intersection of the applied hydrostatic pressure and the hydrostatic yield stress curves. Consistent with our finite element calculations, matrix yielding in the SCS6/Ni$_3$Al composite
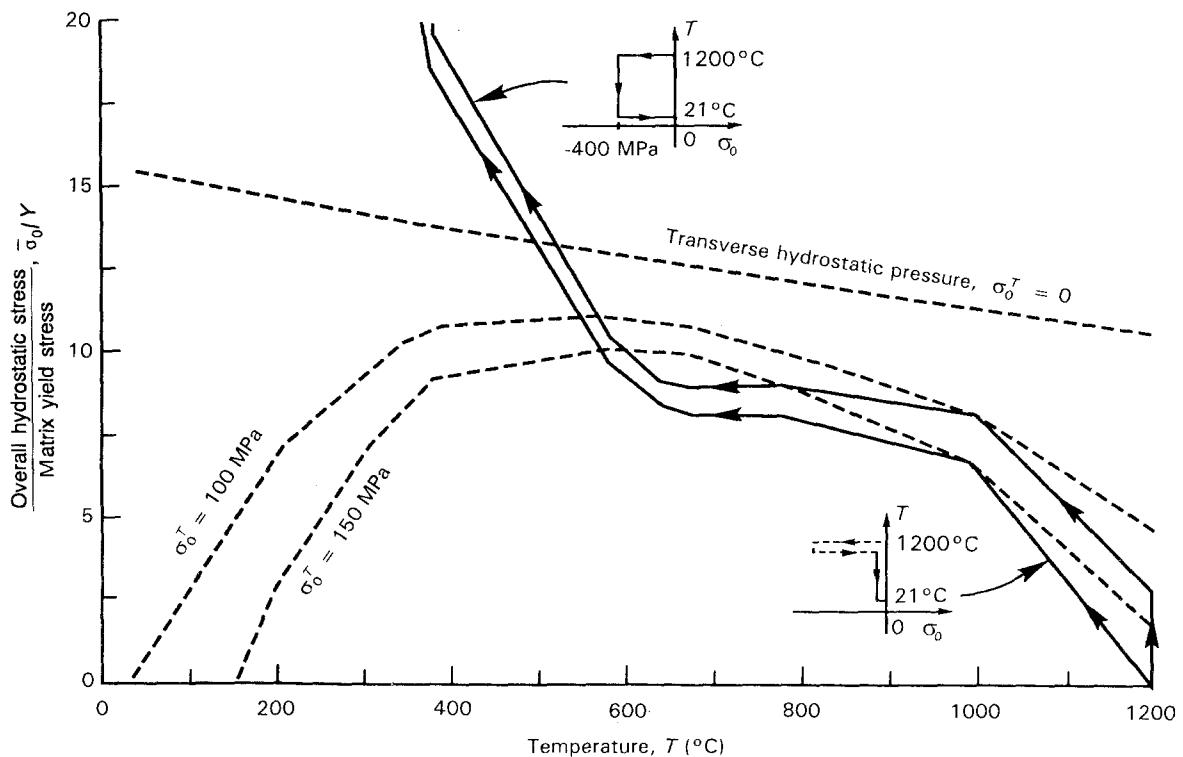

Figure 27 Variation of the (———) hydrostatic yield stress and (———) HIP equivalent hydrostatic pressure with temperature for the uncoated SCS6/Ni$_3$Al composite.
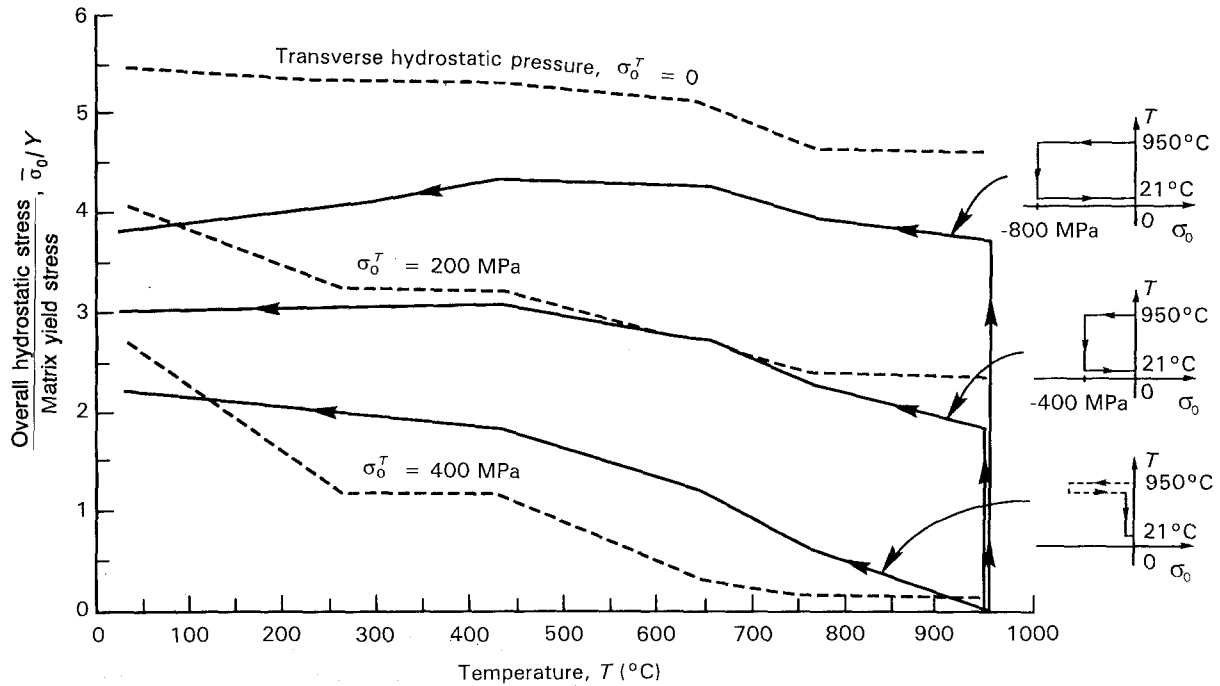
Figure 28 Variation of the (– – –) hydrostatic yield stress and (———) HIP equivalent hydrostatic pressure with temperature for the uncoated SCS6/Ti$_3$Al composite.

can be induced earlier in the HIP process by maintaining the hydrostatic pressure, σ_0, during cooldown to room temperature. As we found earlier, this causes redistribution of the local stresses and leads to reduction of the magnitude of the matrix stress. It is also clear that increasing σ_0 translates the applied load curve in Fig. 27 upwards in the direction of the hydrostatic yield stress curve. In this case, initial yielding of the composite takes place at a higher temperature during the cooldown path, which may further reduce the magnitude of the local stresses. The actual onset of yielding will be different from that indicated in Fig. 27 if a more refined stress field is employed. The self-consistent estimate of the initial yield stress for the SCS6/Ti$_3$Al composite reveals no yielding during the HIP regimes shown in Fig. 28. On the other hand, our calculations with the PHA model and the finite element method indicated plastic yielding in this system for some of the HIP paths. The conclusion drawn from Fig. 28 is that initial yielding can be induced earlier in the process by modifying the HIP path such that cooldown to room temperature takes place at a constant, high pressure.

Another modification of the HIP path which may improve the local stresses, is the superposition of an isotropic stress, σ_0^T, in the transverse plane of the composite, as in Section 5.3. In this case, the loads applied consist of the hydrostatic stress, S, caused by the temperature change, the hydrostatic pressure, σ_0, and the overall transverse hydrostatic stress, $\bar{\sigma} = [0 \, \sigma_0^T \, \sigma_0^T \, 0 \, 0 \, 0]^T$. Substituting into Equation 17, and using the Mises yield function (Equation 7), the hydrostatic initial yield stress is found as

$$S_Y^{*r} = [Y - \sigma_0^T(B_{22}^r + B_{23}^r - 2B_{12}^r)]/$$

$$(B_{11}^r + 2B_{12}^r - B_{21}^r - B_{22}^r - B_{23}^r) \qquad r = 1, N$$

$$(20)$$

It is seen from Equation 20 that the magnitude of the initial yield hydrostatic stress is reduced by superimposing the transverse isotropic pressure, σ_0^T. Equation 20 is plotted in Figs 27 and 28 for selected magnitudes of σ_0^T, where the stress concentration factors were found with the self-consistent method. The onset of yielding was found at the intersection of the applied load curve and the S_Y^{*r} curve. The actual yield temperature depends on the magnitude of the isotropic pressure, σ_0^T, maintained during the process, and it can be elevated substantially by increasing σ_0^T. These observations indicate how the processing parameters contribute to earlier, more extensive plastic straining, and thus to reduction of residual stresses.

6. Conclusion

Adverse thermal residual stresses generated during fabrication of fibrous composites can be reduced by a CVD carbon coating. The fibre coating provides a buffer that reduces the fibre/matrix constraint and the stresses caused by thermal mismatch of the phases. However, the coating may cause higher concentrations of certain stress components under mechanical loading. This is true, in particular, for the matrix hoop stress at the interface with the coated fibre, under overall transverse normal stress. The magnitude of these effects also depends on the relative stiffness of the matrix, fibre and coating.

Plastic flow of the matrix under overall transverse tension may cause substantial reductions in the tensile interfacial stresses. The implication is that mechanical compatibility in fibrous composites depends not only on the thermomechanical phase properties, but also on the inelastic response of the phases. A reasonably accurate evaluation of thermal residual stresses requires a refined micromechanical model, such as the

PHA model used here. A qualitative assessment of initial yielding during fabrication helps to identify effective HIP regimes, and can be performed with simple micromechanical models, e.g. the self-consistent or Mori–Tanaka schemes.

Numerical evaluations of the local stresses in the two intermetallic composites indicate that significant reductions in thermal residual stresses after hot isostatic pressing can be achieved by modifying the processing path. Most of the reductions in the adverse stresses in the matrix were obtained when cooldown to room temperature took place at a constant pressure. Increased pressure helped reduce the local stresses.

Another modification found effective in relieving the matrix residual tensile stresses is the application of axial compression which is smaller than the transverse hydrostatic pressure. The matrix axial tensile stress was found to be smallest when the overall axial stress was absent. In this case, the magnitudes of the fibre axial stress and the radial stress at the interface were also reduced, but remained compressive at the end of the HIP cycle. While decreasing the overall axial pressure relative to the transverse hydrostatic pressure caused significant reductions in the axial stresses and radial stresses in the phases, it also enhanced the matrix tensile hoop stress slightly. The smallest matrix hoop stress was found under three-dimensional hydrostatic pressure.

Thermal residual stresses generated in composite materials have a profound effect on their performance in service. In particular, the residual stresses may reduce or enhance the local stresses developed in the phases under service loads. The differences in the residual stresses after fabrication by variable HIP parameters, however, have a minor effect on the final stress states.

Acknowledgements

References

1. R. HILL, *J. Mech. Phys. Solids* 13 (1965) 189.
2. T. MORI and K. TANAKA, *Acta Metall.* 21 (1973) 571.
3. Y. BENVENISTE, *Mech. Mater.* 6 (1987) 147.
4. Y. BENVENISTE, G. J. DVORAK and T. CHEN, *ibid.* 7 (1989) 305.
5. G. J. DVORAK, Y. A. BAHEI-EL-DIN, R. S. SHAH and H. NIGAM, in "Inelastic Deformation of Composite Materials", edited by G. J. Dvorak (Springer, New York, 1990) p. 270.
6. G. J. DVORAK and Y. A. BAHEI-EL-DIN, *Acta Mech.* 69 (1987) 219.
7. R. HILL, *J. Mech. Phys. Solids* 15 (1967) 79.
8. G. J. DVORAK and J. L. TEPLY, in "Plasticity Today: Modeling, Methods and Applications", W. Olszak Memorial Volume, edited by A. Sawczuk and V. Bianchi (Elsevier Science, Amsterdam, 1985) p. 624.
9. J. L. TEPLY and G. J. DVORAK, *J. Mech. Phys. Solids* 36 (1988) 29.
10. S. NEMAT-NASSER, T. IWAKUMA and M. HEJAZI, *Mech. Mater.* 1 (1982) 239.
11. J. ABOUDI, *Solid Mech. Arch.* 11 (1986) 141.
12. G. J. DVORAK, *Proc. R. Soc. Lond. A* 437 (1992) 311.
13. Y. A. BAHEI-EL-DIN and G. J. DVORAK, in "Metal Matrix Composites: Testing, Analysis, and Failure Modes", ASTM STP 1032, edited by W. S. Johnson (American Society for Testing and Materials, Philadelphia, PA, 1989) p. 103.
14. G. J. DVORAK, in "Metal Matrix Composites", Vol. 2, "Mechanisms and Properties", edited by R. K. Everett and R. J. Arsenault (Academic Press, Boston, 1990) p. 1.
15. Y. A. BAHEI-EL-DIN, G. J. DVORAK and R. S. SHAH, in "Computational Experiments", ASME PVP, Vol. 176, edited by W. K. Liu, P. Smolinski, R. Ohayon, J. Navickas and J. Gvildys (American Society for Mechanical Engineers, New York, 1989) p. 125.
16. Y. A. BAHEI-EL-DIN, R. S. SHAH and G. J. DVORAK, in "Mechanics of Composites at Elevated and Cryogenic Temperatures", ASME AMD, Vol. 118, edited by S. N. Singhal, W. F. Jones and C.T. Herakovich (American Society for Mechanical Engineers, New York, 1991) p. 67.
17. G. J. DVORAK, Y. A. BAHEI-EL-DIN, Y. MACHERET and C. H. LIU, *J. Mech. Phys. Solids* 36 (1988) 655.
18. H. NIGAM, G. J. DVORAK and Y. A. BAHEI-EL-DIN, *Int. J. Plasticity*, 10 (1994) 23.
19. *Idem. ibid.* 10 (1994) 49.
20. Y. A. BAHEI-EL-DIN, G. J. DVORAK, J. LIN, R. S. SHAH and J. F. WU, "Local Fields and Overall Response of Fibrous and Particulate Metal Matrix Composites" Final Technical Report, Alcoa Laboratory, Contract 379 (52R)053(22L), November 1987.
21. "ABAQUS User's Manual" (Hibbit, Karlsson and Sorensen, Providence, RI, 1989).
22. Y. A. BAHEI-EL-DIN, in "Thermal and Mechanical Behavior of Ceramic and Metal Matrix Composites", ASTM STP 1080, edited by J. M. Kennedy, H. H. Moeller and W. S. Johnson (American Society for Testing and Materials, Philadelphia, PA, 1990) p. 20.
23. G. J. DVORAK, T. CHEN and J. L. TEPLY, *Compos. Sci. Technol.* 43 (1992) 347.
24. R. HILL, *J. Mech. Phys. Solids* 12 (1964) 199.
25. P. M. NAGHDI, in "Plasticity, Proceedings of the Second Symposium on Naval Structural Mechanics" (Pergamon Press, 1960) p. 121.
26. R. S. SHAH, PhD thesis, Rensselaer Polytechnic Institute, Troy, NY (1991).
27. Y. F. DAFALIAS and E. P. POPOV, *J. Appl. Mech.* 43 (1976) 645.
28. R. J. DIEFENDORF, private communication (1990).
29. N. S. STOLOFF, *Int. Mater. Rev.* 34 (1989) 153.
30. F. H. FROES, C. SURYANARAYANA and D. ELIEZER, *J. Mater. Sci.* 27 (1992) 5113.
31. M. MITTNICK, *SAMPE J.* 26 (1990) 49.
32. N. S. STOLOFF and D. E. ALMAN, *Mater. Sci. Eng.* A144 (1991) 51.
33. Y. A. BAHEI-EL-DIN and G. J. DVORAK, in "Damage and Oxidation Protection in High Temperature Composites", Vol. 2, ASME AD, Vol. 25-2, edited by G. K. Haritos and O. O. Ochoa (American Society for Mechanical Engineers, New York, 1991) p. 21.
34. G. J. DVORAK, *J. Appl. Mech.* 53 (1986) 737.
35. *Idem, Proc. R. Soc. Lond.* A431 (1990) 89.
36. Y. A. BAHEI-EL-DIN, *Int. J. Plasticity* 8 (1992) 867.
37. G. J. DVORAK, *J. Thermal Stresses* 15 (1992) 211.
38. G. J. DVORAK and Y. A. BAHEI-EL-DIN, *J. Appl. Mech.* 49 (1982) 327.